nature reviews earth & environment

https://doi.org/10.1038/s43017-023-00508-8

Review article

Check for updates

Monitoring Earth's climate variables with satellite laser altimetry

Lori A. Magruder[1,2] ✉, Sinead L. Farrell[3,4], Amy Neuenschwander[2], Laura Duncanson[3], Beata Csatho[5], Sahra Kacimi[6] & Helen A. Fricker[7]

Abstract

Satellite laser altimetry measures accurate elevations of the Earth's surface and precise changes with time, monitoring key climate variables. These observations have transformed understanding of the Earth System, revealing changes and dynamics across spheres. In this Review, we highlight the Earth and climate science contributions from three NASA satellite laser altimeter missions: Ice, Cloud and land Elevation Satellite (ICESat; 2003–2009), ICESat-2 (2018 to present) and Global Ecosystem Dynamics Investigation (GEDI; 2018 to present). Over two decades of observations, satellite altimetry revealed cryosphere decline, including a loss of 320 Gt yr^{-1} in global land ice from Greenland and Antarctica, and a 30% decrease in volume of winter sea ice in the Arctic between 2003 and 2021. Observations have also been key to understanding ecosystems on land, providing data on the hydrosphere (showing that 57% of the Earth's seasonal terrestrial water storage variability comes from human-managed reservoirs) and biosphere (showing that forest carbon stocks have globally increased owing to growth, despite a loss of the equivalent of ~8 Gt CO_2 from land use). In the atmosphere, the data have enabled assessment of the global vertical cloud distribution, aerosol fraction, and dust and smoke transport. There is currently no planned satellite laser altimeter mission to continue from ICESat-2 and GEDI, jeopardizing critical data collection that supports decision-making and environmental management.

Sections

[1]Department of Aerospace Engineering and Engineering Mechanics, University of Texas at Austin, Austin, TX, USA. [2]Center for Space Research, University of Texas at Austin, Austin, TX, USA. [3]Department of Geographical Sciences, University of Maryland, College Park, MD, USA. [4]Department of Atmospheric and Oceanic Science, University of Maryland, College Park, MD, USA. [5]Department of Geological Sciences, University at Buffalo, Buffalo, NY, USA. [6]Jet Propulsion Laboratory, California Institute of Technology, Pasadena, CA, USA. [7]Institute of Geophysics and Planetary Physics, Scripps Institution of Oceanography, University of California San Diego, La Jolla, CA, USA. ✉e-mail: lori.magruder@austin.utexas.edu

Key points

- NASA's three satellite laser altimeter missions (ICESat, GEDI and ICESat-2) have provided surface elevation data for monitoring essential climate variables across the Earth system, at high spatial and temporal resolution.
- In the cryosphere, ICESat and ICESat-2 observations revealed a decline in sea ice thickness in the Arctic and a loss of land ice from glaciers, the Greenland Ice Sheet and the Antarctic Ice Sheet, and provided insights into the drivers of loss.
- In the biosphere, ICESat, ICESat-2 and GEDI measured vegetation structure and ground heights across all ecosystems to better quantify changes to the biosphere in response to climatic and anthropogenic forces.
- In the hydrosphere, ICESat, ICESat-2 and GEDI inventoried and monitored global water reservoirs and sea level changes including in the Arctic Ocean. ICESat-2 provides nearshore bathymetry for benthic mapping and coastal geomorphology.
- In the atmosphere, ICESat and ICESat-2 have provided vertical structure of global clouds and aerosol layers critical to modelling radiative fluxes. They have also revealed substantial climate events associated with dust storms and fire disturbances.

Introduction

Understanding interactions between Earth system components — the biosphere, atmosphere, cryosphere, hydrosphere and geosphere — is key to quantifying how conditions might change in the future, and what role humans play in such change. Therefore, improving the ability to monitor these components and predict Earth system evolution is an urgent scientific and societal need. One way to monitor the health of the Earth system is through continuous observations of key climate variables[1], such as land and sea surface temperatures, and greenhouse gas concentrations.

Many essential climate variables are measured in terms of their surface height. For example, changes in ice-sheet elevation have indicated ice mass loss leading to sea level rise[2]. Thinning sea ice increases the exchange of heat, moisture and momentum between the ocean and atmosphere and lowers surface albedo through various positive feedbacks that amplify polar climate change[3]. Variations in forest canopy height and structure indicate aboveground biomass stocks, a proxy for carbon storage[4]. Water height in lakes and reservoirs indicates the availability of global water resources[5]. By measuring elevation data all across the Earth system at a resolution, accuracy and precision not achievable by other sensors, satellite laser altimetry has provided a multidecadal record of global height change with time[6], enabling these variables to be tracked.

Since the early 2000s, NASA has led three Earth-observing satellite laser altimetry missions (Table 1). The Ice, Cloud and land Elevation Satellite (ICESat; 2003–2009)[7] and ICESat-2 (2018 to present)[8] had the primary objective of monitoring the surface heights of ice sheets, glaciers and sea ice to determine how the cryosphere is responding to a changing climate. Global Ecosystem Dynamics Investigation (GEDI) (2018 to present)[9] was designed to make precise measurements of forest canopy height, canopy vertical structure and ground surface elevation, with the primary science motivation of better understanding the role of forests in the terrestrial carbon cycle. Twenty years have elapsed since ICESat was launched, allowing for the long-term monitoring of 14 key climate variables across many surface types (Fig. 1). Now, these measurements have begun to reveal a collection of dynamic processes and feedbacks where the atmosphere, ocean, land, cryosphere and biosphere interact across various spatial and temporal scales[6].

In this Review, we present the science discoveries enabled by monitoring climate variables with NASA's three satellite laser altimetry missions. We begin by reviewing the history of satellite altimetry since the 1970s, and the technical advances achieved since satellite laser altimeters were first used for Earth observation in the early 2000s. Then, we discuss knowledge gained from satellite laser altimetry on climate-related spheres: cryosphere, hydrosphere, biosphere and atmosphere, placing an emphasis on cryosphere and biosphere, as both are directly representative of the science requirements of the three missions highlighted here. We close by setting an agenda for the future, advocating for sustained satellite laser altimeter missions to ensure continuous data acquisition to address critical questions in Earth Science.

Background

This section summarizes the basic principles and provides a brief history of satellite radar and laser altimetry since 1975.

Basic principles of altimetry

Satellite altimetry is based on a measurement principle of precise timing combined with knowledge of the satellite positioning and orientation to retrieve Earth surface elevation data[10]. Altimeters transmit short pulses of electromagnetic waves, and the receiver records the arrival of the surface reflection. The time interval between pulse transmission and return reflection determines the range between the sensor and the surface. This basic measurement is the two-way time delay (T), which is converted into a range (R) using $R = cT/2$, where c is the propagation velocity of electromagnetic waves in free space, otherwise known as the speed of light[11].

Range values are converted to a surface height (h) above a reference ellipsoid as a function of geodetic position (latitude ϕ and longitude λ)[12] determined by the position vector of the altimeter and the pointing vector of the laser (Box 1 figure, panel a). Range corrections are applied to account for instrumental errors, atmospheric effects, and geophysical factors (Box 1 figure, panel b). The altimetry calculation, providing $h(\phi,\lambda)$ from R, is performed for all data. As the spacecraft moves in its orbit, the altimeter measurements describe ellipsoidal height profiles or transects of the surface topography via an aggregation of elevations along the satellite ground track.

Satellite altimeters have different instrument technologies and approaches to determine precise timing of the surface reflection and subsequent derivation of range, depending on the frequency of the transmitted energy and the signal detection technique. Past and present laser altimetry missions have used both full-waveform[13] and photon-counting technology[14] (Box 1 figure, panel c).

Early radar altimetry

Satellite radar altimetry for Earth observation was first implemented in two missions: NASA's Geodynamics and Earth Ocean Satellite (GEOS-3) mission in 1975, and the 3-month Seasat mission in 1978[15]. GEOS-3 and

Seasat carried altimeters optimized for the oceans and ultimately led to a branch of ocean remote sensing with missions such as TOPEX/Poseidon and Jason[16]. However, their coverage (±65° and ±72.16°) also led to usable data over ice in Greenland[17] and Antarctica[18], serving as the first demonstration of polar altimetry. These missions demonstrated satellite altimetry as a technology poised for Earth science beyond oceanography[19].

Improved radar altimetry designs by the European Space Agency (ESA) for measurements over ice followed as the Earth Remote Sensing (ERS) satellites. ERS-1 extended latitudinal coverage of the polar regions to ±81.5° and had two modes of operation (ocean and ice). ERS-1 and follow-on missions (ERS-2 and Envisat) provided an invaluable time series of changes over ice sheets[20] and established that variability Arctic sea ice thickness was dominated by changes in the length of the summer melt season[21]. However, radar altimetry had limitations over ice, especially over steep terrain[22], where the surface slope combined with large radar footprints (~3 km) and coarse spatial resolution (~340 m along track) created challenges. It also encountered a loss of signal over complex topography[23], penetration of the radar signal into the surface layers[24] and biases in terrain height retrievals in the presence of vegetation[25]; and the latitudinal limit of coverage (±81.5°) excluded measurements of the oldest, multiyear sea ice in the high Arctic[26] and a large part of the Antarctic Ice Sheet.

Early laser altimetry

Knowledge gained from the three ESA radar altimetry missions over ice was the foundation for continued pursuit of cryospheric observations with improved radar technology onboard CryoSat-2[27]. It motivated NASA to pursue laser altimetry in the mid-1990s to acquire elevation time series to understand the effects of climate change in the polar regions. The Geoscience Laser Altimeter System (GLAS), the planned instrument onboard the first Earth-observing laser altimetry satellite mission, began development in the early 1990s.

GLAS was launched on ICESat in January 2003. ICESat's primary mission objective was to detect changes in ice-sheet elevations as small as 1.5 cm yr^{-1}, spatially averaged over areas of 100 × 100 km, with secondary objectives for retrievals of cloud height and aerosol distribution, sea ice and terrain height[28]. The GLAS design was optimized for operation over the ice sheets, with a smaller footprint diameter (~70 m), minimal surface (water, snow, ice) penetration (infrared laser wavelength), and higher vertical accuracy than its radar predecessors. The data acquisition strategy focused on ensuring higher spatial resolution (172-m sampling along elevation profiles) and global coverage in a near-polar orbit observing areas between ±86° latitude, capturing the majority of Earth's glacial and sea ice[28]. GLAS used a 1,064-nm wavelength laser[7], and atmospheric measurements used a 532-nm wavelength made possible by frequency-doubling the near-infrared altimeter channel[29]. However, owing to technical issues[30] including the loss of the 532-nm channel in 2006, the mission operational plan was modified and ICESat operated in a 'campaign mode', where repeat-track data were acquired during the 33-day sub-repeat of a 91-day repeat orbit two to three times per year[7] (September 2003 until October 2009)[31].

Despite the altered operational adjustments, ICESat was an overall success and provided precise elevation data to the Earth science community. Under optimal conditions of flat, reflective surfaces, ICESat elevations presented a precision of 3 cm (ref. 32) and a geolocation accuracy of better than 4.5 m (ref. 33). Over land ice, ICESat revealed ice mass loss from mountain glaciers[34], Antarctica and Greenland[35], and Antarctic ice shelves[36], and detected active subglacial lakes in Antarctica[37]. ICESat tracked a net decline of ~0.6 m in multiyear sea ice thickness in the Arctic between 2003 and 2008[38] but indicated little interannual variability in the thickness and volume of Southern Ocean sea ice[39].

ICESat/GLAS was not specifically designed to measure the vertical structure of terrestrial ecosystems, and the 33-day seasonal campaigns led to limited spatial coverage; however, the satellite did perform a series of off-nadir pointing manoeuvres to densify the data collected over forested ecosystems. The resulting data from dense tropical and temperate forests provided the first comprehensive assessment of global surface and canopy heights to inform biomass estimates[40]. These data underscored the necessity of global measurements of vegetation structure[41–43]. The ICESat mission also provided information on cloud fraction[29] atmospheric structure and aerosols[44] and inventoried inland water bodies[45]. ICESat established methodologies and technologies for satellite laser altimetry that informed concepts for future missions.

Table 1 | Operational and instrumental parameters of NASA's space-based laser altimeter systems

Parameters	ICESat	ICESat-2	GEDI
Altitude (mean value)	596 km	500 km	420 km
Coverage	±86°	±88°	±51.6°
Number of beams	1	6	4
Laser wavelength	532 nm/1,064 nm	532 nm	1,064 nm
Lidar technology	Full-waveform	Photon-counting	Full-waveform
Laser repetition rate	40 Hz	10 kHz	242 Hz
Along-track sampling	172 m	0.7 m	60 m
Laser footprint diameter	35–70 m[a]	11 m	25 m
Laser energy per pulse	70 mJ	0.03 mJ/0.12 mJ[b]	5 mJ/10 mJ[b]
Laser pulse width	4 ns	1 ns	14 ns
Orbit inclination	94°	92°	51.6°
Track separation at Equator	15 km	<2 km after 3 years	Variable
Ground track repeat cycle	91 days	91 days	N/A
Mission geolocation accuracy requirement	4.5 m	6.5 m	10 m

[a]ICESat had variable laser footprint diameters for each of the operational lasers. [b]ICESat-2 and GEDI provide two energy levels across the multiple beams.

Modern laser altimetry missions

Building on the success of the ICESat mission and in response to the 2007 Decadal Survey for Earth Science and Applications from Space from the National Academies of Sciences, Engineering and Medicine[46] on priority climate observations, NASA readied two complementary laser altimeter systems for launch in 2018: ICESat-2[8] and GEDI[9]. ICESat-2 carries the Advanced Topographic Laser Altimeter System (ATLAS), a photon-counting altimeter[47]. ICESat-2 was placed in a near-polar orbit to extend latitudinal coverage to ±88° and partially fill a gap in cryosphere observations by reducing the size of the 'pole hole'[48]. The GEDI technology, ideal for vegetation studies, leverages the heritage

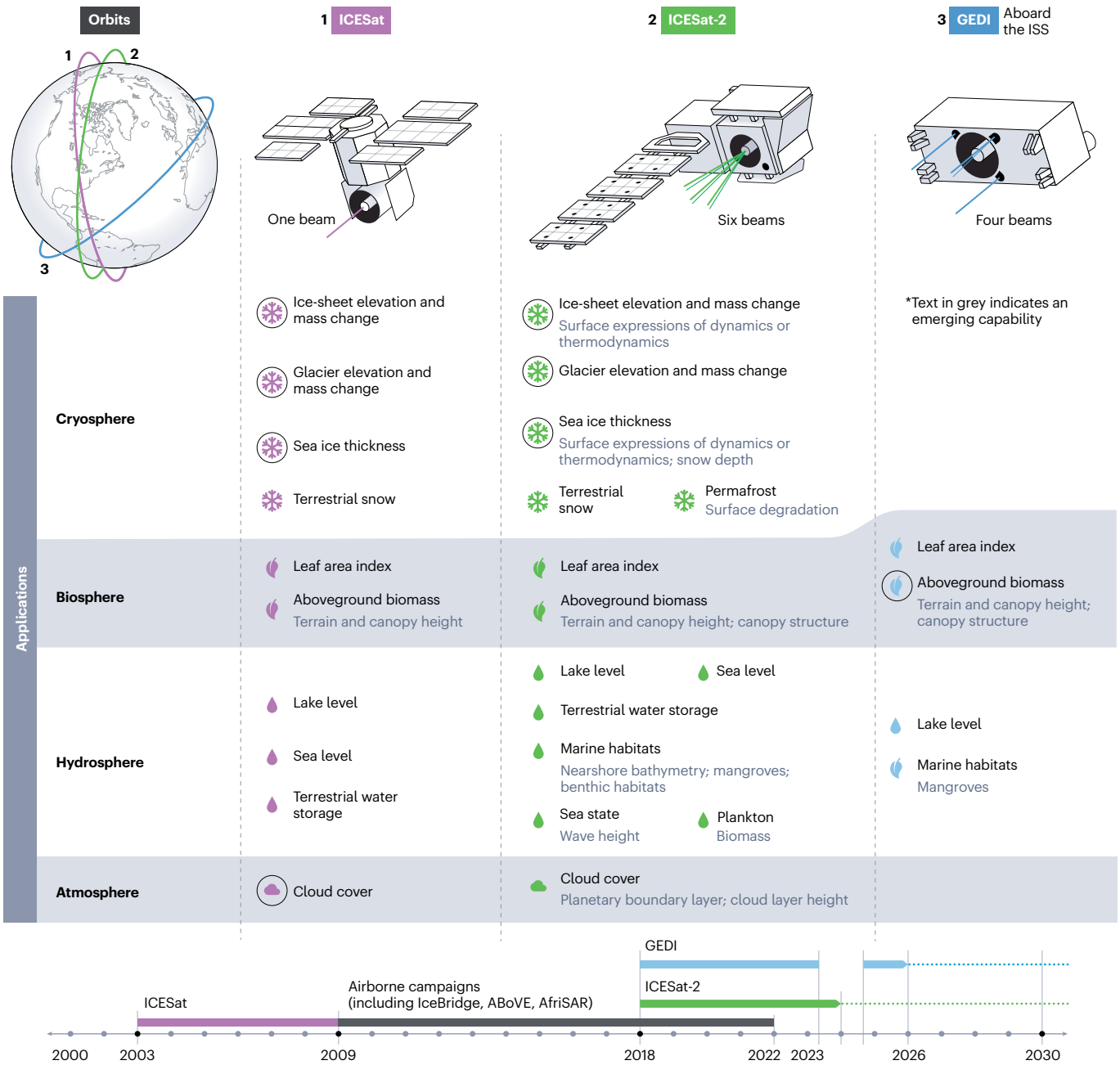

Fig. 1 | Key climate variables monitored by satellite laser altimetry. Observations from the Ice, Cloud and land Elevation Satellite (ICESat), ICESat-2 and Global Ecosystem Dynamics Investigation (GEDI) across the cryosphere, biosphere, hydrosphere and atmosphere aid measurements of a wide variety of essential climate variables including ice-sheet and glacier elevation and mass change, sea ice and terrestrial snow thickness, permafrost, leaf area index, aboveground biomass, lake and sea level, terrestrial water storage, sea state, marine habitat properties, plankton and cloud cover. Climate variables that map to a specific mission science requirement are circled. ISS, International Space Station.

of full-waveform lidar similar to GLAS[9]. GEDI was placed on the International Space Station (ISS) with an orbit extending between ±51.6° and a primary measurement requirement of sampling the 3D structure of forested ecosystems[9]. Although using different detection technologies, both laser altimeters collect data with multiple beams in configurations that optimize coverage. The multiple beam design mitigates the large uncertainties in the estimates of elevation change resulting from the correlation between surface slope and elevation change during non-exact repeat measurements for a single beam[49].

ICESat-2 has similar science objectives to ICESat, with ice-sheet and sea ice measurement requirements. Specifically, the goals are to quantify ice-sheet elevation change to estimate contributions to sea

level change and identify the driving mechanisms, and quantify changes in sea ice thickness to investigate ice–ocean–atmosphere interactions[8]. Secondary scientific goals are associated with vegetation structure, as ICESat-2 provides global coverage and high vertical accuracy over terrestrial ecosystems, including boreal forests at high northern latitudes that are not measured by GEDI owing to the orbital constraint of the ISS[50]. ICESat-2's mid-latitude collections are complementary to GEDI's tropical and temperate coverage, and the high-latitude coverage of ICESat-2 creates the opportunity to create global vegetation structure products derived from the collective measurements of the two missions[8].

Evaluation of ICESat-2's elevation retrievals demonstrated measurements with a higher resolution, accuracy and precision than

Box 1

Basic principles of satellite laser altimetry

Full-waveform

Full-waveform laser altimetry, used in ICESat/GLAS and GEDI, records all of the reflected energy from each transmitted laser pulse to create a returned energy profile along the laser line of sight[10]. This received energy profile creates a waveform whose shape and size depends on the vertical structure of the illuminated surfaces, the surface reflectivity and the topography. An advantage of full-waveform systems is that the data processing required for elevation and geolocation determination is well understood[219]. The waveform has a single peak for simple, unvegetated surfaces with low slopes, most ice sheets and the ocean; the average range to the surface is from the centroid of the transmit pulse to the centroid of a Gaussian fit to the waveform[9] (see the figure, panel **b**). However, more complex surfaces and vegetation lead to multiple peaks in the waveform, due to the laser illuminating multiple surfaces at different elevations[13] (see the figure, panel **b**). A range offset for each individual surface can be derived from the timing of each peak relative to the time-tag of the waveform leading edge. Full-waveform signal detection relies on thresholds of thousands of photons returning to the receiver, which requires a large amount of transmitted energy[10]. This requirement on laser power for signal detection constrains the possible repetition rates of the laser, which affects the along-track resolution. GPS, Global Positioning System; POD, precise orbit determination.

Photon-counting

Photon-counting laser altimetry, used in ICESat-2/ATLAS, removes the dependence on signal thresholds, as its detection sensitivity is at the single-photon level[47]. Each individual photon is assigned a time-tag to calculate the range based on the laser energy time of flight, and standard methods are used to provide a geodetic position and elevation[220]. Single-photon systems eliminate the need for substantial laser power, allowing the laser to operate at higher repetition rates and the energy from a single laser to be distributed across multiple beams (see the figure, panel **c**). These operational aspects of photon-counting systems provide expanded coverage and improve the resolution of the along-track measurement. One challenge of photon-counting laser altimetry is that the detector records all incoming photons but does not distinguish between true signal and ambient solar noise, so that complex algorithmic approaches are required for signal finding when processing the data[14].

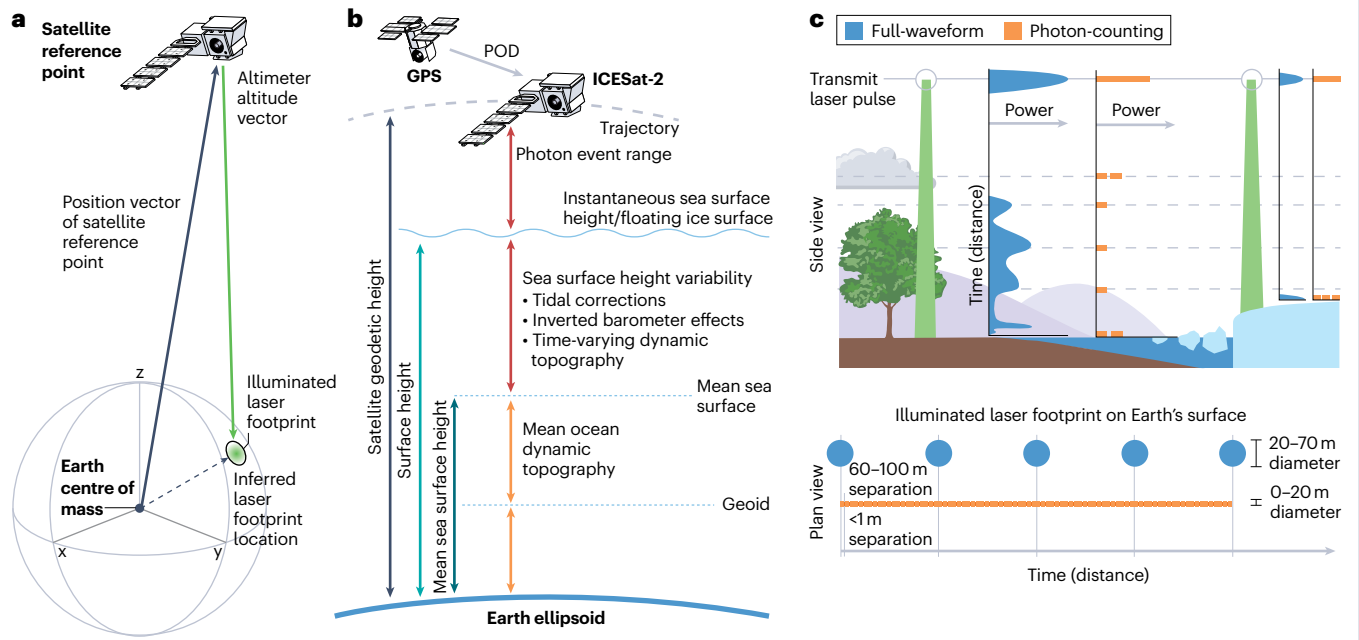

previous satellite altimeters. Calibration field experiments on the Antarctic plateau[51] showed an elevation accuracy better than 3 cm with a precision of 9 cm (1-sigma standard deviation). Over flat surfaces such as Arctic sea ice leads, early results demonstrated an along-track surface height precision of ~2 cm at kilometre length scales[52], and subsequent analysis showed that a further improvement, to ~1-cm height precision, was achievable with specialized processing[53]. Canopy height retrievals are better than 5 m RMSE (root mean squared error), and terrain elevations often have RMSE values better than 1 m (ref. 54) in most ecosystems; with improvements to the data products, those accuracies will continue to improve. Going beyond mission requirements, the 532-nm wavelength of ICESat-2's ATLAS penetrates clear non-turbid water as deep as ~50 m to allow estimation of water depths in the nearshore zones[55] and in melt ponds on ice shelves[56] and sea ice[53].

Over vegetated regions, GEDI is providing a new perspective of forest structure at a global scale, with RMSE for height retrievals of nominally ~2 m at 25-m length scales[57], and forest products not previously available from satellite altimeters, including canopy cover, plant area index (which is similar to leaf area index, LAI), foliage height diversity and aboveground biomass. The spatial sampling from GEDI has provided orders of magnitude more 3D forest structure measurements than GLAS, enabling a wide range of forest mapping and monitoring studies[50].

Cryosphere

The cryosphere is a global climate regulator, playing a critical role in Earth's energy budget, and is a major contributor to sea level change[58]. The loss of ice from the sea and land drives climate processes by decreasing albedo, altering heat and moisture fluxes and raising sea level, and is therefore critically important to understand. However, there is great uncertainty over the future of ice mass loss across the cryosphere[59]. Satellite altimetry uniquely provides the vertical dimension crucial for estimating volume change by measuring sea ice thickness, elevation and mass change of land ice (ice sheets, ice shelves and glaciers), and terrestrial snow depth, all essential climate variables (Fig. 1). This section discusses how satellite altimetry has advanced the study of processes of sea ice and land ice change (Fig. 2), enabling more accurate representation of these variables in climate models.

Sea ice

Sea ice extends across ~4–6% of the ocean annually and exhibits strong seasonal variability[60]. Historically, observations were limited to mainly ship-based measurements[61], submarine-based upward-looking sonar[62] and aerial surveys[21,63], resulting in a lack of routine observations. Spaceborne passive microwave radiometry revealed an average annual global decline in sea ice extent of ~1.5% per decade between 1979 and 2013[60], but this technique cannot track changes in ice thickness and mass flux. Satellite altimetry has transformed the understanding of the sea ice thickness distribution and its variability by routinely measuring sea ice surface topography, including ice floe and lead heights[6,21]. A detailed picture of sea ice thickness and volume change over time has emerged[64], enabling the investigation of interactions with ocean processes[65].

In particular, ice thickness information is sought after to improve short-term forecasting[66] and is playing an increasingly important role in climate monitoring and prediction, as the thickness distribution integrates both the thermodynamic and dynamic processes that control ice growth and decay[65]. ICESat observations provide unambiguous measurements of both sea ice freeboard (the height of floating ice floes above local sea level) and sea level in areas of open water within the fractured ice pack (called leads)[67]. Ice thickness, the relevant climate variable, can be inferred from sea ice freeboard, using assumptions about the depth of snow blanketing the sea ice, and snow and ice densities[38].

Arctic Ocean. Arctic sea ice has transitioned from predominantly thick, multiyear sea ice that survives summer melt to first-year ice that is thinner and seasonal in nature and now accounts for ~70% of the ice cover compared with ~35% in 1985[68]. The rate of sea ice loss in the Arctic is accelerating, altering ocean stratification, affecting weather patterns and ecosystems, and affecting human activities[69]. In the Arctic Ocean, ICESat extended observations to +86° N and provided the first opportunity to track both the seasonal and interannual variability in sea ice freeboard[70].

ICESat observations revealed a marked decline in winter sea ice freeboard of ~1.6 cm yr^{-1} in the Arctic between 2003 and 2008, mainly over the older, multiyear ice[70]. Between March 2004 and March 2008, this multiyear ice thinned by ~0.6 m, resulting in an estimated total volume loss of 6,300 km^3 (ref. 38). Following a then record-setting minimum ice extent in September 2007[71], ICESat recorded pronounced ice thickness losses during the 2007/2008 winter season[38]. These losses increased the net ocean–atmosphere heat flux[72] and were observed in both the satellite laser and radar altimeter records[26]. By the end of winter 2012, Arctic sea ice volume had declined by a further 1,479 km^3, discovered when the ICESat-era record was combined with complementary measurements from the radar altimeter on CryoSat-2[73]. ICESat-2 continued the observational record and revealed a total winter ice volume loss of ~6,000 km^3 over the 18-year period between 2003 and 2021, equivalent to ~33% of total Arctic sea ice volume in winter[64].

Satellite laser altimetry can also contribute to better understanding of the geophysical processes driving the observed sea ice variability, owing to its high spatial resolution and temporal sampling. For example, ICESat-2 data have been used to map complex sea ice topography in finer detail than from earlier satellite altimeters and have provided additional measurements of the ice properties needed to track processes that control sea ice thermodynamics (advance and retreat) (Fig. 2a) and dynamics (drift and deformation)[53]. ICESat-2's small footprint and dense along-track sampling can also be used to map the evolution of ice properties during the winter growth period[74] and summer melt season[75]. These measurements have enabled process-driven research including analysis of ice surface roughness and mapping sea ice ridging intensity in the Arctic Ocean[76], assessing the lead width distribution[53] and detecting features of summer melt[77] (Fig. 2a). Simultaneous retrieval of the ice thickness distribution with such high-resolution observations of sea ice properties will ultimately improve understanding of time-varying sea ice processes.

Southern Ocean. After decades of gradual increase, Antarctic sea ice coverage has been declining since 2014[78]. In the Southern Ocean, ICESat enabled the first altimetry-based estimates of sea ice freeboard (Fig. 2b) and thickness[79], where radar altimetry techniques are hindered by deeper snow, frequent flooding, and complex snow and ice stratigraphy[80]. When combined with snow depth estimates from passive microwave sensors, ICESat showed that ice in the Weddell Sea had a complex seasonal cycle, with average ice thickness ranging from ~1.3 m in austral fall, to ~2.3 m in austral spring and ~1.6 m in austral summer[81]. ICESat observations for the period 2003–2008[39] also showed that

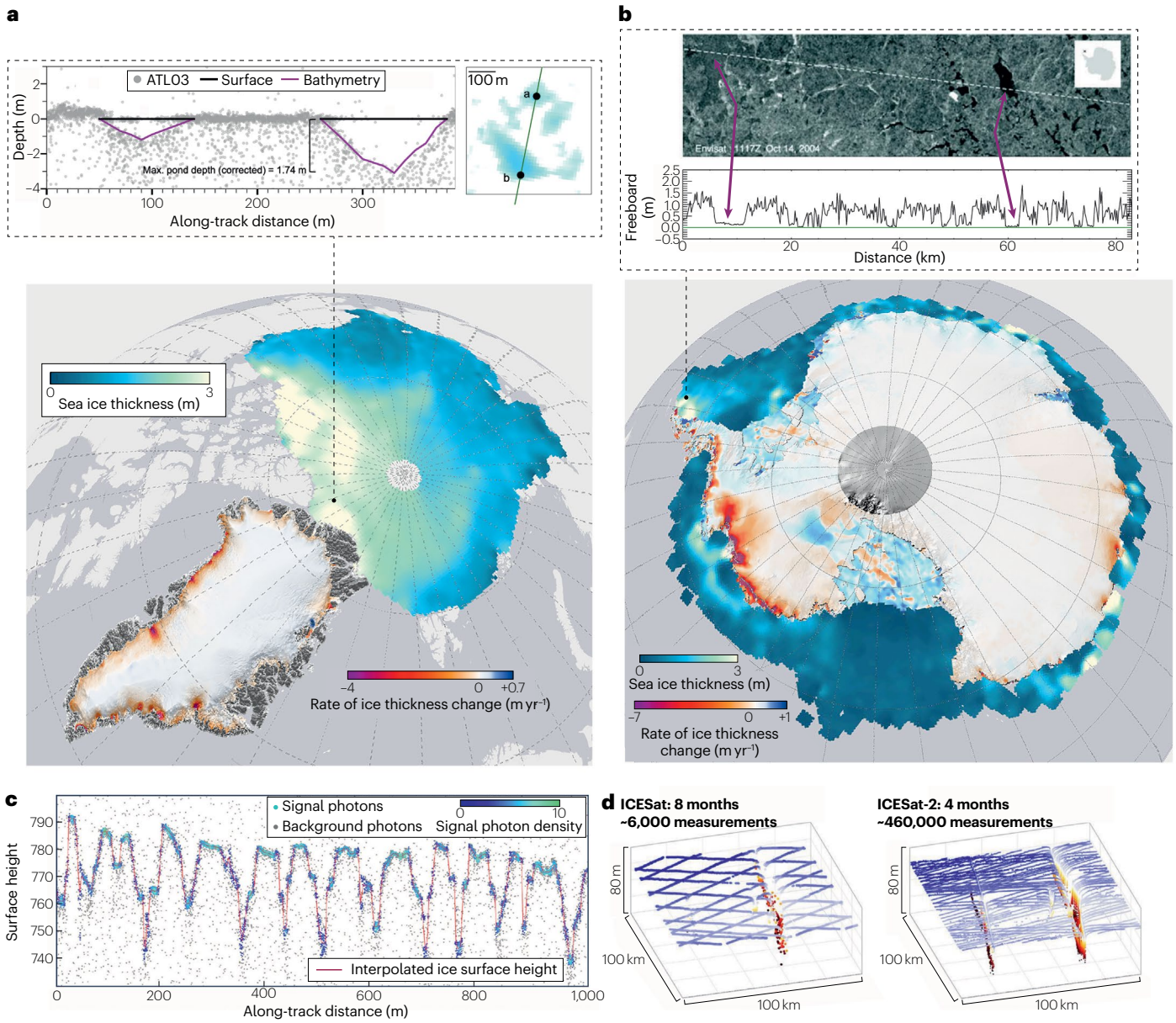

Fig. 2 | Changes in sea ice and land ice in the polar regions from ICESat and ICESat-2. Main maps show sea ice thickness for the Arctic and Greenland region (sea ice thickness for January 2020[64]) and the Antarctic region (average for April to November 2019)[82] from ICESat-2. The height change rate for the land ice sheet is also shown, based on data from ICESat to ICESat-2 (ref. 49). Inset panels show details of processes made possible with high-resolution ICESat-2 data. **a**, Melt pond bathymetry and depth on Arctic sea ice in June 2019 from ICESat-2 with near-coincident Sentinel-2 Multi-Spectral Instrument image of surface ponding[53]. **b**, Sea ice freeboard in October 2004 from ICESat with near-coincident Envisat ASAR image of sea ice conditions[79]. The ICESat ground track is shown as a dashed line. In the small inset map of Antarctica, × marks the approximate geographical location of the image and the ICESat profile. Flight direction is from left to right. Pink arrows indicate leads. Solid green line indicates interpolated sea surface height[79]. **c**, Sermeq Kujalleq (Jakobshavn Isbræ) recorded by a single ground track of ICESat-2 ATL03 data and analysed with the density-dimension algorithm for ice surfaces[216]. **d**, Rift on Ross Ice Shelf as seen in ICESat GLA12 and ICESat-2 ATL06 data[49]. Part **a** is adapted from ref. 53, CC BY 4.0 (https://creativecommons.org/licenses/by/4.0/). Part **b** is adapted with permission from ref. 79, Wiley. Part **c** is adapted from ref. 106, Elsevier. Part **d** is adapted with permission from ref. 49, AAAS.

circumpolar ice volume peaked in austral spring, averaging ~11,111 km^3. A comparable estimate based on ICESat-2 for austral spring 2019 was ~10,062 km^3 (ref. 82). Year-round observations from ICESat-2 show that the observed seasonality in ice thickness is probably explained by a mixture of competing processes (snowfall, snow redistribution, snow ice formation, ice deformation, and basal growth and melt) in different parts of the divergent Antarctic ice cover[82]. ICESat-2's high-resolution measurements have also contributed new insights about wave penetration into the marginal ice zone[83] and the prevalence of under-ice phytoplankton in the Southern Ocean[84]

Land ice

Land ice, including the Antarctic and Greenland ice sheets[85], glaciers and icecaps (GIC)[86], is losing mass at an accelerating rate contributing to global sea level rise[59]. During the last century (1901–2018), sea level rise was dominated by ocean thermal expansion and glacier melt; however, by 2008–2016, the recent rapid increase of ice-sheet mass loss made land ice the largest contributor[59,85,87,88]. By monitoring the elevation change patterns, satellite altimetry missions enable the estimation of ice-sheet and GIC mass balance evolution, provide insights into ice dynamics, identify regions of potential instabilities[89], and investigate active subglacial hydrology[37].

Antarctic and Greenland ice sheets. ICESat and ICESat-2 measurements have provided changes in land ice elevation since 2003[49] (Fig. 2). ICESat along-track data from 2003 to 2008 showed that there was overall loss of land ice mass from the grounded portions of Antarctica, especially in the Amundsen Sea embayment in West Antarctica where some glaciers thinned more than 9.0 m yr^{-1}, and Greenland where thinning rates of fast flowing glaciers averaged 0.84 m yr^{-1} (ref. 35). A similar analysis was carried out for Antarctica's floating ice shelves and showed that the grounded ice changes correlate with ocean-driven ice-shelf thinning[36]. However, the temporal averaging and single beam profiling was insufficient to inform about underlying processes.

In Greenland, ICESat observations combined with Operation IceBridge airborne laser altimetry allowed for outlet glacier-scale studies of dynamic thickness change, revealing significant spatiotemporal variations[90] and glacier response to changes in ocean heat[91]. For a longer-term view, ICESat was used to co-register the precise digital elevation model (DEM) generated from historical aerial photographs for the entire Greenland margin[92]. ICESat observations also provided model input data, such as for estimating the elastic component of vertical crustal deformation[93] and for transient numerical models of ice flow[94].

On ice shelves, advection of features introduces noise into the elevation data, which can be removed with knowledge of the ice velocity in a Lagrangian approach. This approach was used to derive basal melt rates for Filchner Ronne and Ross ice shelves[95]. ICESat repeat-track data gave important information about smaller dynamic features, including ice fronts[96]; grounding zones[97] and grounding-zone migration[98]; basal channel growth[99]; and active subglacial lakes in Antarctica[37,100]. These ICESat repeat-track results led to a science requirement for ICESat-2 for dynamic features.

ICESat-2 extended the elevation record from ICESat, enabling an estimate of ongoing mass loss from both ice sheets between 2003 and 2019, amounting to 320 Gt yr^{-1} (14 mm sea level rise)[49] (Fig. 2). This comprehensive analysis covering all ice sheets (grounded and floating ice) confirmed the theoretical link between thinning ice shelves and grounded ice loss[101], and demonstrated a connection with competing ocean and atmosphere processes. The ongoing record also allows for estimation of long-term trends, as well as seasonal and annual variability[102,103].

ICESat-2 data provide a means of assessing the different surface-mass-balance and firn-densification models that are critically important for estimating mas balance from altimetry observations[104]. The top-of-snow measurement detects elevation changes that can be attributed to snow accumulation, and enables linking to driving processes[103]. For example, monthly height changes over the West Antarctic Ice Sheet during 2019 showed that large height increases occurred in winter[105]. By using climate reanalysis data, a large percentage (41%) of these signals was attributed to short-duration extreme precipitation events, with 63% associated with atmospheric rivers, which occurred only 5.1% of the time.

Many key ice-sheet processes act on short spatial scales (1–10 km), and ICESat-2 data are the first with sufficiently high spatiotemporal resolution to resolve the evolution of the dynamic features associated with these processes, such as crevasses[106] (Fig. 2c), rifts (Fig. 2d), ice fronts[107] and iceberg calving[108], grounding-zone migration since ICESat[109] and on tidal timescales[110], basal channels[111,112], dolines[113], thinning at pinning points[114] and active subglacial lakes[115]. ICESat-2's 532-nm photons penetrate standing water, allowing estimates of meltwater depth from raw photon data[56]. Although ICESat-2's limited spatial coverage prevents complete surface meltwater mapping, the technique has the potential for enhancing meltwater depth estimates from satellite imagery[116].

Glaciers and icecaps. GIC are contributing significantly to sea level rise, and are vital for the hydrological cycle and for freshwater supplies. ICESat data have been combined with other historic or contemporaneous datasets to track annual and decadal mass changes in GIC for the epoch 2003–2009. Combining ICESat, GRACE (Gravity Recovery and Climate Experiment) and GPS also enabled separation of glacier mass loss effects from crustal deformation and water storage trends, improving mass change estimates of Alaskan glaciers[117]. Overall, the glaciers in the Arctic, Canada, Alaska, coastal Greenland, the southern Andes and High Mountain Asia (HMA) together contributed 259 Gt yr^{-1}, ~30% of the sea level rise signal, and as much as the ice sheets[34]. ICESat also enabled detection of regional patterns of change; it revealed significant and widespread glacier mass loss in the eastern, central and southwestern parts of the Hindu Kush–Karakoram–Himalaya region, resulting in a total annual mass loss of 13 Gt yr^{-1} (ref. 118). In Greenland, annual mass loss was 41 Gt yr^{-1} for the icecaps and peripheral glaciers, with the highest mass loss in the southeast[119]. The three major archipelagos of the Russian High Arctic lost mass at a rate of 9 Gt yr^{-1}, with most of this loss driven by climate change rather than ice dynamics[120]. In Svalbard, comparison of ICESat observations with historic DEMs (1965–1990) revealed a connection between glacier mass balance and latitude and the dynamical behaviour of the individual glaciers[121].

Regional comparisons between ICESat and ICESat-2 enabled analyses of smaller, more complex regions undergoing change and detected accelerating thinning in several glaciated regions, including the peripheral GIC surrounding the Greenland Ice Sheet[122]. Although they covered only 4% of Greenland, these GIC currently provide 11% of Greenland mass loss, and this loss doubled between the ICESat and ICESat-2 periods; mass loss from northern peripheral glaciers increased by a factor of 4 (ref. 122). Similar analyses in Svalbard showed that thinning increased over most regions[123], with the highest negative rates along the west coast and areas bordering the Barents Sea, linked to Arctic warming over the last decades and increasing thinning in eastern Svalbard, correlating with atmospheric and oceanic warming[124]. In HMA, glaciers thinned with an average rate of 0.34 m yr^{-1} from 2003 to 2019[125]. The temporal sampling of ICESat-2 has enabled detailed studies of the seasonal behaviour of glacier regions. For example, in HMA, seasonality was observed in three categories, linked to regional atmospheric conditions (to Westerly and Monsoon)[126].

ICESat-2's dense spatial sampling and accurate elevation measurements over rugged terrain make it suitable for assessing DEM elevation accuracy[127] and calculating elevation changes by differencing DEMs and ICESat-2 elevations. The latter approach was applied to detect

elevation changes in the Rongbuk Glacier catchment on the northern slope of Mt Qomolangma (Mt Everest)[128]. The fine-scale resolution of the ICESat-2 data has also enabled detailed studies of small-scale outlet glacier features in Greenland and Svalbard, such as crevasses[106] (Fig. 2c).

Biosphere

Terrestrial vegetation is tightly linked to climate change, with vegetation absorbing around one-third of annual fossil fuel emissions through growth. In contrast, deforestation causes ~1.8 GtC yr^{-1} of emissions[129]. Mapping, monitoring, and forecasting vegetation carbon flux are fundamental for understanding the impacts of climate change and land use on the global carbon cycle. Laser altimetry can provide detailed and accurate 3D vegetation structure measurements at a spatial resolution required for management[130].

Land topography and vegetation height

Vegetation height[40] and underlying topography[131] are measured directly by satellite laser altimetry, and the reflected waveforms or photon clouds enable estimation of a suite of other ecologically important attributes, including climate-critical vegetation aboveground biomass (AGB)[50], which consists of approximately 50% carbon. Data from ICESat/GLAS provided the first global synoptic measurements of terrain and vegetation height from space; those data then factored into global digital elevation products[131] and canopy height products[132]. The large footprint diameter of ICESat/GLAS, however, created challenges in decoupling terrain and canopy heights from the returned waveform, particularly in areas with topographic slope more than 10°[133,134]. ICESat-2 and GEDI's designs addressed this limitation, and GEDI's smaller footprints have been used for a suite of height mapping products, both alone and through data fusion with Sentinel-2 data[135], Landsat[136] and TanDEM-X[137,138]. ICESat-2 and GEDI data have also been combined for height mapping where both datasets are available[139], although caution should be taken to resolve discrepancies between the datasets before they are combined[57,140].

GEDI and ICESat-2 each have strengths and limitations for mapping canopy height and terrain structure. As GEDI was designed primarily for vegetation, its more powerful lasers can penetrate even the densest canopies, thus providing particularly new data in areas such as dense tropical forests where GLAS measurements were sparse and ICESat-2 often cannot accurately resolve height[141]. GEDI combines ground and canopy photons in waveforms, and algorithms are used to estimate the ground elevation from the lower portion of each waveform. In contrast, the high laser repetition rate on ICESat-2 creates a nearly continuous profile along the surface for each beam. As a result, ICESat-2 classifies photons as reflecting from both the terrain and canopy surface, separately. ICESat-2's photon classification has highest accuracies in sparse to moderate canopy covers in short-stature vegetated systems as demonstrated in Europe[142] and North American boreal forests[143]. Both GEDI and ICESat-2 datasets have higher uncertainties in terrain elevation over steep slopes[144], and dense and sparse canopies.

Another benefit of laser altimetry is the detection of the terrain beneath the vegetated layer. In particular, both ICESat-2 and GEDI have recorded water levels of inundated forests in the Amazon[145,146], and accurate terrain heights of peatlands[147]. Although the measurement techniques are different between GEDI and ICESat-2, they show similar patterns with retrieval accuracies impacted by terrain slope and to a lesser extent canopy cover[148].

Ecosystem structure and biomass

Leaf area index (LAI) and vegetation AGB are two additional essential climate variables that can be derived from laser altimetry. LAI can be estimated with laser altimetry based on the vertical gap probability of foliage at discrete heights[149]. LAI represents the crown foliage content and is used to drive ecosystem models to estimate photosynthesis, carbon exchange with the atmosphere, and interception of precipitation and microclimate variables[150]. Biomass cannot be directly resolved from altimetry, but it is related to 3D volume and is often empirically derived from laser altimetry[151].

ICESat/GLAS data were used independently, or in combination with other remote sensing data, to produce early ecosystem structure and AGB products representative of 2010 AGB stocks[42], and estimated carbon emissions[43]. They have also been combined with other remotely sensed data products including interferometric synthetic aperture radar (SAR) to map mangrove heights and AGB[152], and optical Landsat imagery to create disturbance products to estimate forest recovery rates[153], canopy fuels[154], and canopy cover[148].

GEDI and ICESat-2 data have been used to update these earlier products for both mapping and monitoring changes in forest structure, which are essential for understanding how and where the terrestrial biosphere is mitigating climate change through storage and sequestration of carbon as biomass. GEDI data have been used to map forest carbon stocks[4] at a range of spatial scales: globally at 1-km resolution[50], for continental wall-to-wall mapping with fusion with Sentinel-2[155], and national mapping[156]. GEDI-domain forests have been predicted to host ~480 Pg of AGB[50]. Approximately 26% of GEDI-domain AGB is currently stored in global protected areas, and GEDI data were used to estimate that these areas have prevented an additional 9.65 Pg of carbon emissions over the past two decades, equivalent to roughly 1 year of global annual fossil fuel emissions[157].

GEDI and ICESat-2 data have also been integrated with data from optical sensors to monitor changes in forest structure over time, including estimation of forest fuels[158], and forest recovery from disturbance, including fire[159], logging[160] and charcoal degradation[161]. Additionally, space-based laser altimetry data has been used to map forest diversity at a range of scales[162], including structural diversity in the United States[163], in Europe[164] and pantropically[165]. Structure has been linked to habitat to study ecology[166], such as mapping predator–prey relationships[167] and bird species distributions[168].

Finally, data are being incorporated into ecosystem models to forecast future forest carbon fluxes, answering critical questions related to whether forests will continue to act as a net sink of carbon or become carbon sources[169] due to increasing pressures from land use and climate change. GEDI data are limited in that the ISS orbit does not pass over high northern latitudes, including boreal forests which are warming faster than other ecosystems on the planet. However, ICESat-2 data were used to produce the first 30-m laser-altimetry-based map of AGB for boreal forests across the entire circumpolar region[170] (Fig. 3) and, when combined with GEDI's tropical and temperate AGB estimates, complete a global accounting of AGB for the current era.

Hydrosphere

The hydrosphere encompasses all water on Earth, including surface water in lakes, rivers and reservoirs, groundwater, and oceans. Satellite altimetry is useful in monitoring the hydrosphere (Fig. 1), owing to its spatial coverage and repeat period for seasonal change assessment, its small footprint diameter for capturing small water bodies, and its ability to penetrate the canopy for measurements within flooded forests and

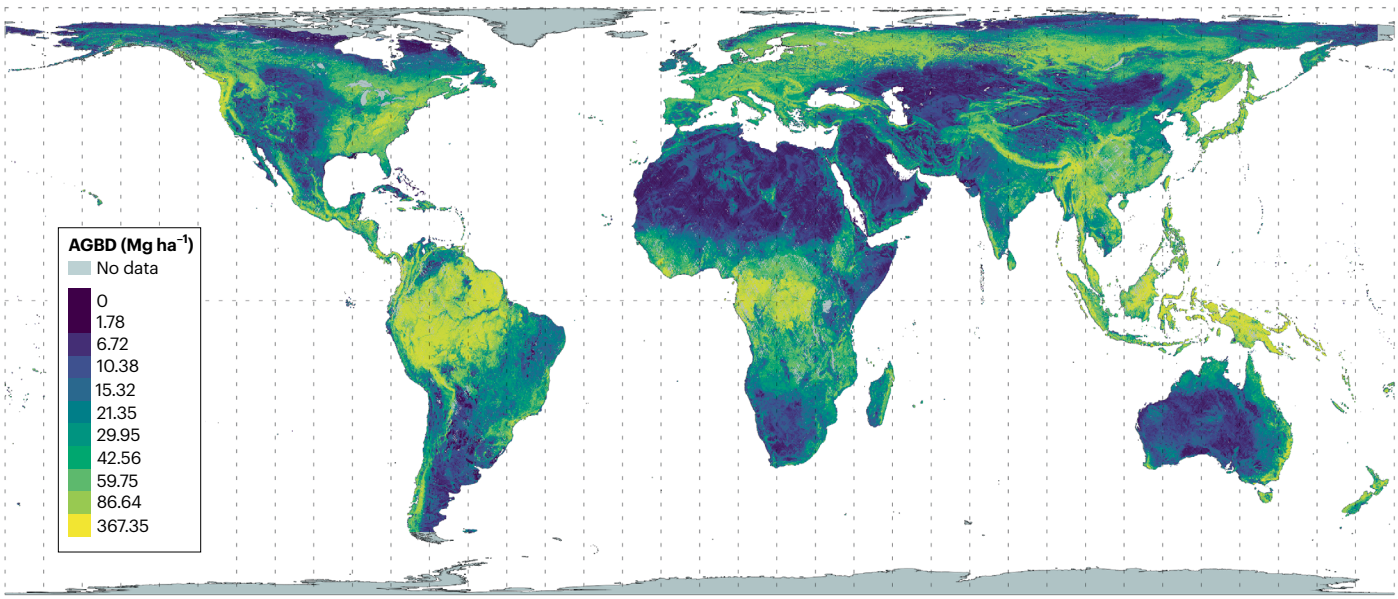

Fig. 3 | Global woody aboveground biomass density (AGBD) from GEDI and ICESat-2. Estimates up to 52° N are from the 1-km gridded GEDI product, whereas northern ecosystems have wall-to-wall 30-m maps from a fusion of ICESat-2, Harmonized Landsat/Sentinel-2 and the Copernicus digital elevation model. Both products are available through the NASA Oak Ridge National Laboratory DAAC (https://daac.ornl.gov/).

wetlands[171] (Fig. 1). Applications include monitoring the dynamics of coastlines[172], the boundaries of lakes and rivers[173], water surface slope[174] and an emerging application from ICESat-2: nearshore bathymetry[175]. This section discusses these applications.

Inland water

Monitoring the temporal and spatial distribution of terrestrial water storage is crucial for effective water resource management and decision-making[176]. In situ networks have supported management of individual reservoirs and are used to determine river water elevation levels and water surface slope, but they are limited in scale and limited in inaccessible remote areas[5,177]. ICESat, GEDI and ICESat-2 data can be used in global, homogeneous, perennial monitoring of terrestrial water (including lakes, rivers and reservoirs). For example, the combination of ICESat and ICESat-2 observations has enabled the retrieval of long-term net water volume trends across the 2003–2023 time period for more than ~94% of global lake volume, revealing an overall water storage increase of 10.88 ± 16.45 Gt yr^{-1} (ref. 178).

ICESat data were used to locate lake levels across more than 500,000 unique locations for the entirety of the mission lifetime[45], to produce a new inventory that increased the understanding of global hydrological resources. The ~70-m ICESat footprint improved sampling of water bodies and provided the first space-based measurements over bodies of water that were previously omitted by radar altimetry owing to its larger-diameter footprint[179]. Monitoring seasonal and abrupt changes in inland water levels was possible with ICESat[180] at some locations, although the general lack of repeat measurements over most water bodies limited the utility of ICESat data for seasonal characterization. Instead, the observations supported the analysis of individual geographical location measurements at a single point in time for validation of hydrodynamic models[45] and advanced model simulations of discharge and flow velocity[177]. ICESat allowed reservoirs to be better understood at a global level[45], but the sparse track spacing was insufficient to enable a comprehensive assessment of water resources.

ICESat-2's smaller footprint size and frequent sampling allowed for even smaller reservoirs to be mapped and monitored on seasonal timescales[181]. Merging ICESat-2 reservoir retrievals with existing databases to examine 227,386 water bodies during the period from October 2018 to July 2020 revealed that human-managed reservoirs provide 57% of Earth's seasonal terrestrial water storage variability, and that the seasonal variation in water levels is much larger than the signal for natural water bodies (0.86 m versus 0.22 m)[173], establishing a baseline for tracking human modifications to the global hydrological cycle. River network monitoring efforts also leverage the multibeam observations and smaller footprint diameter of ICESat-2, capturing water surface slope information that is essential for estimating reach-scale discharge and flow dynamics[174]. Evaluation of 815 reaches in Europe and North America sampled by ICESat-2 using independent data led to a value of 23 mm km^{-1} as the median absolute error in water surface slope for 89% of the reaches investigated[174]. This small amount of error indicates that ICESat-2-derived slopes can be used as a global solution in place of local assessments using tide gauges.

Analysis of GEDI and ICESat-2 data for inland water studies revealed ICESat-2 elevation biases to be ~0.05 m and GEDI biases ~0.26 m. Nevertheless, the combined datasets improve overall water level retrievals in terms of accuracy and temporal resolution[182] while capturing the variability of the monthly, seasonal and annual cycles for use in predicative climate models[183].

Sea level

Satellite laser altimetry can directly monitor sea level, including in coastal regions and the polar oceans, extending the datasets from oceanographic satellite radar altimetry missions such as TOPEX/Poseidon and Jason. Indeed, mean sea surface heights from ICESat

showed the feasibility of generating a global sea surface height product, albeit with an overall elevation bias of −10.0 ± 1.0 cm with respect to TOPEX/Poseidon owing to the uncorrected sea state bias in the ICESat data and different interactions of the radar and laser energy with the ocean[184]. Gaps in temporal coverage[30] ultimately limited ICESat's ability to recover interannual trends in global sea surface height.

ICESat's higher latitudinal coverage (±86°) compared with TOPEX/Poseidon (±66°) enabled the production of a new satellite-only mean sea surface model for high northern latitudes that was used to map mean dynamic topography in the persistently ice-covered Arctic Ocean[185]. ICESat measurements of sea surface height in the Arctic Ocean were also inverted to determine gravity anomalies[186], which were used to generate a more detailed and accurate satellite-only marine gravity field that revealed important new tectonic features, particularly in the Amerasian and Eurasian basins[187]. In the Southern Ocean, ICESat data were used to fill in the gap in tide models around Antarctica through retrieval of tidal variations on ice shelves[188] and ultimately used to improve Antarctic tide models[189].

Coastal bathymetry

Sea level rise leads to changes in coastal geomorphology[190]; yet there was a major gap in nearshore bathymetry measurements due to limitations in sensor coverage and logistical complications associated with accessing remote locations until 2018[175]. ICESat-2's unique capability to penetrate clear non-turbid water as deep as ~50 m provided water depth estimates in the nearshore zone and seamless topographic-bathymetric profiles across the waterline, which has transformed coastal hydrosphere studies[175]. Although the ICESat-2 seafloor height retrievals can be used independently for coastal applications, the data are often combined with relative depths from multispectral optical images to transform the bathymetry maps to an absolute vertical scale. This satellite-derived bathymetry combines the high vertical accuracy of the ICESat-2 measurements with the wide spatial coverage of the imagery[55] (Fig. 4).

Satellite-derived bathymetry with ICESat-2 has led to important work in characterizing the coastal ecosystem, as the repeat coverage and data quality from ICESat-2 allows scientists to capture geomorphological change across timescales that were not possible before the launch of the mission[191]. It also furthers the understanding of benthic habitat health and life cycles such as coral reef bleaching and seagrass degradation[192]. This application has been extended to mangroves and tidal flats, as the full coastal seascape is critical to the livelihood of local communities and contains nearly 25% of the oceanic carbon pool[55].

Atmosphere

Clouds and aerosols are fundamental components of Earth's atmosphere and its radiative impact, and their significance extends to weather, climate, and air quality. Satellite laser altimetry contributes to understanding cloud cover, aerosols, and the planetary boundary layer (PBL) by providing accurate information on vertical structure, composition, properties and dynamics[193] (Fig. 1). The accurate vertical information provided by altimetry has enhanced our understanding of these atmospheric components and their interactions, progressing climate modelling and environmental monitoring[194].

Cloud cover and aerosols

Clouds have a critical role in maintaining the planet's energy balance through reflection of solar radiation and heat retention[195]. Laser altimetry enables accurate measurements of cloud top heights and cloud layer thickness, providing a better understanding of cloud cover and its impact on the Earth's energy flux[195].

ICESat's design to observe the atmosphere centred on the goal of global coverage with sufficient sensitivity to fill the gaps introduced by passive instruments for height distribution and accurate extinction and absorption information[29]. Once on-orbit, ICESat provided instantaneous observations of atmospheric vertical structure, and dual wavelength channels allowed for identifying cloud and aerosol layer boundaries and optical thickness. Both channels allowed for resolving extinction and backscatter cross-sections as a measure of radiative properties (Fig. 5); the 532-nm photon-counting detectors provided higher spatial resolution, and the 1,064-nm analog detection had lower spatial resolution but a wider dynamic range[30].

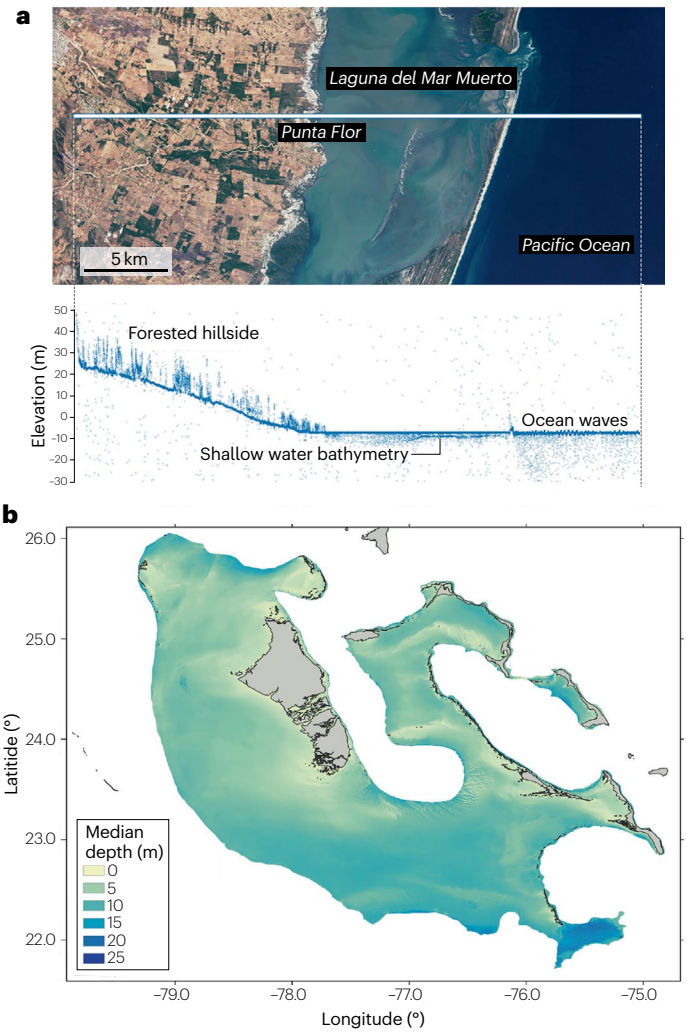

Fig. 4 | Nearshore shallow water bathymetry mapping with ICESat-2. a, An ICESat-2 transect of measurements across the coast of Mexico as the satellite moves from the left to the right. The corresponding photon elevations (bottom graph) reveal vegetation, water surface, shallow water bathymetry and ocean waves. **b**, Satellite-derived bathymetry model of depths over the Great Bahama bank using a single Landsat image and ICESat-2 bathymetry[217]. Part **a** is adapted from ref. 217, CC BY 4.0 (https://creativecommons.org/licenses/by/4.0/).

ICESat made important contributions for climate modelling by determining cloud overlap statistics, which represent the extent to which different layers of the atmosphere interact. These statistics have a major influence on the rates of heating and cooling in the atmosphere, but are often assumed parameterizations or simplified equations, without rigorous physical basis[44]. In autumn 2003, for example, ICESat quantified the global vertical distribution of cirrus clouds, a key component of the terrestrial radiative balance in the stratosphere, confirming the dynamics of convection in relation to the tropopause (mean altitude of 14.5 km in the tropics and 9.5 km in the northern mid-latitudes; the peak location of deep convection around 7.5° N; and the average thickness of cirrus clouds at ~1.6 km)[196].

ICESat-2 continues to provide the vertical profiles of clouds and aerosols for an altitude of 0–14 km (the vertical range window is slightly truncated because of the high repetition rate of the laser[197]). Although challenging for a single-wavelength system, ICESat-2 can discriminate between clouds and aerosol constituents through backscatter characteristics of the laser energy, layer heights and horizontal homogeneity[198]. Additionally, ATLAS measures tenuous atmospheric layers composed of blowing snow or high optically thin cirrus clouds that are extremely important to climate models and often difficult to detect[199]. Tenuous atmospheric layers are potentially the most important to Antarctica and Arctic radiative forcings, but they also have a strong influence on humidity and heat flux in the tropics given the high frequency of cirrus.

ICESat's atmospheric channel also provided context for the surface measurements in the sense of how the atmosphere affects the accuracy of surface elevation measurements. Scattering of the laser energy in the presence of clouds, aerosols and blowing snow can lengthen the energy path length and lead to a range delay[200]. This 'forward-scattering' bias is a strong function of the receiver field of view (FOV) and grows as the FOV increases, making the effect bigger for ICESat but still affecting ICESat-2 by introducing elevation uncertainties of the order of 4–6 cm compared with clear sky conditions[201].

Aerosols affect the climate by scattering or absorbing sunlight and participating in cloud formation; they also influence air quality and human health[202]. Satellite laser altimetry helps characterize aerosols by measuring their optical properties, concentrations and spatial distribution, enabling us to study their sources, transport patterns, and influence on air quality and climate[203]. For example, ICESat was used to monitor the transport of the California 2003 forest fire plumes in the northeastern United States[204] (Fig. 5a). This was accomplished by collecting atmospheric profiles across numerous satellite tracks to determine the temporal variations in height of the smoke-induced

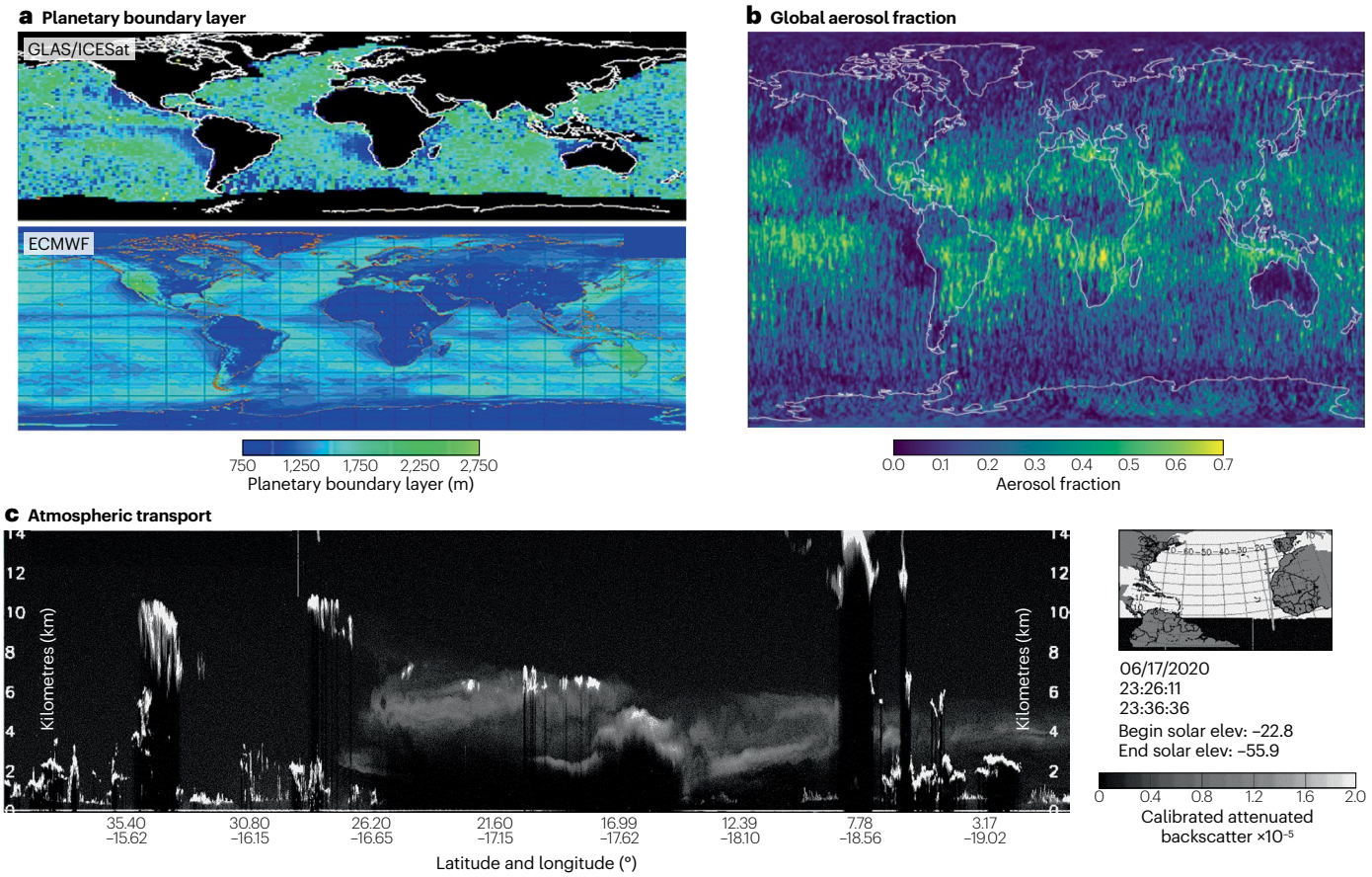

Fig. 5 | The vertical structure of the atmospheric layer from laser altimetry. **a**, ICESat/GLAS backscatter showing the transport of Saharan dust over the subtropical Atlantic to the Caribbean and biomass burning smoke from South Africa to the east coast of South America just south of the Equator. **b**, July 2021 global aerosol fraction from ICESat-2 atmospheric backscatter measurements[198]. **c**, Average height of marine planetary boundary layer (PBL) for October 2003, using the ICESat/GLAS 532-nm backscatter measurements to validate, and the European Centre for Medium-Range Weather Forecasts (ECMWF) PBL height analysis for the same period[218]. Part **a** adapted with permission from ref. 218, Wiley. Part **c** adapted with permission from ref. 197, Wiley.

aerosols, and creating a 4D assessment of the smoke and aerosol propagation over a week to document the initial westward motion and then the direction reversal as a function of interaction with the current weather system[204]. Optical imagery is capable of tracking the aerosol transport but relies on laser altimetry to give the accurate heights of the atmospheric constituents, an important part of understanding aerosol movement and dynamic response (Fig. 5b).

Planetary boundary layer

The PBL is the lowest atmospheric layer and governs the exchange of energy, moisture, and pollutants between the Earth's surface, including both land and ocean, and the upper atmosphere[205]. The PBL hosts all physical interactions between the free troposphere and the surfaces and contains most of the total atmospheric moisture, allowing it to determine the level of convection and storm development[198]. Satellite laser altimetry backscatter can be used to estimate the thickness and height of the PBL, which are its primary physical properties. The backscatter properties reveal the correlated height to where the temperature profile increases abruptly while the relative humidity decreases (Fig. 5c).

These gradients are detected by the laser in terms of the density variability in the reflected signature (backscatter magnitude) using different sensors[206], including ICESat-2[197]. The proportionality between backscatter magnitude and aerosol content for PBL discoveries across seasonal and regional scales is an important part of the future PBL global observing system[207]. Annual PBL height maps from ICESat-2 indicate a height range from 800 m to 1.5 km over oceans without much temporal variability. In contrast, over land, the PBL heights exhibit higher values, typically ranging from 2 to 3 km, with the greatest heights observed over desert and arid regions[198].

Summary and future perspectives

Collectively, NASA's three laser altimeter missions have produced a record of elevation change and structure at multiple spatial and temporal scales for a variety of surface types across the entire Earth system. ICESat captured broad patterns of change in climate variables associated with height to ±86° latitude, recording ice mass loss from mountain glaciers[34], Antarctica and Greenland[35], and sea ice volume loss in the Arctic Ocean[38], and revealing active subglacial lakes in Antarctica[37,100]. It also supported the first estimates of sea ice thickness in the Southern Ocean[39], the first comprehensive assessment of global surface and canopy heights to inform biomass estimates[40], cloud structure information and aerosol detection[29], and an inventory of surface water bodies[176]. ICESat-2 has extended ICESat's time series of observations with continuous, high-resolution along-track measurements of vegetation structure at metre-level length scales and across seasonal cycles[8,49] to 88° latitude. GEDI is providing tropical and temperate canopy heights and terrain mapping, greatly improving the ability to characterize carbon and water cycling, biodiversity and habitat[50] to ±51.6°. These combined records will support the parametrization of these processes and further help to improve the fidelity of Earth system climate models, while also providing benchmark datasets against which to compare future satellite laser altimetry missions.

The evolution of satellite laser altimetry continues as researchers and engineers learn from past missions. The limited spatial coverage is a primary challenge for space-based lasers — the current missions still only measure less than 5% of Earth's surface, given the current sampling strategies and data loss due to cloud cover[208]. Over the ice sheets, comprehensive measurements are needed from the smoother areas to the structurally more complex margins, where the changes are large but the track spacing is too sparse to capture the full details of key processes at the relevant scales[49]. For glaciers, the sparse track spacing at lower latitudes and the angled orientation to the ice flow make height assessments less accurate[209]. Over sea ice, accurate delineation and measurement of leads and sea ice pressure ridges is required for assessment of changes in ice mass balance, and the retrieval of such properties remains challenged by the current sensor resolution[210] and the presence of clouds, while the penetration of meltwater ponds on sea ice in summer limits the retrieval of ice thickness during the melt season[77]. The long latency of sea ice data products prohibits their usage by international ice services and for weather forecasting, which require near-real-time information[74].

Vegetation monitoring by laser altimetry also has faced limitations, as both GEDI and ICESat-2's vegetation height and AGB accuracies are negatively affected by slopes. Additionally, the geolocation uncertainty of GEDI data is relatively large for laser altimetry (~10 m)[211], which complicates high-resolution fusion between GEDI and datasets obtained from SAR and optical sensors[137], as well as validation efforts with airborne lidar and field datasets. As geolocation of GEDI data improves over time, substantial refinements are seen in forest structure and height products[212]. Some of the limitations in spatial coverage can be overcome through fusion of GEDI and ICESat-2 data, extending information at high northern latitudes where GEDI data are unavailable[142]. An ideal laser altimetry mission for vegetation would include enough beams (or scanning capabilities) to provide a mapping capability with sufficient sampling to capture important subannual dynamics of phenological cycles.

Looking forward, for land ice, the sampling must be at least seasonal, to capture the mass loss processes driving the changes (such as iceberg calving and ice-shelf basal melting) in the most dynamic regions of the ice sheets and glaciers. To meet operational needs in sea-ice-covered waters, improve predictive capability and track synoptic variability, daily-to-weekly sampling of sea ice concentration, thickness and velocity across both the polar and subpolar seas and their marginal ice zones should be provided with low latency. Emerging techniques[213] that use dual-band radar altimetry seek to improve estimates of snow depth on sea ice, which is essential for measuring sea ice thickness and estimating mass balance.

In future missions, the observations should ensure global coverage and provide canopy height estimates with accuracies of 1–2 m at the 1-hectare scale. Combining terrain and canopy height measurements with other satellite datasets, such as multispectral imagery and SAR, will help to reduce the uncertainty of global carbon stocks and provide other information necessary for quantifying biodiversity, habitat fragmentation and forest management[133]. Spatially explicit maps of aboveground biomass and carbon fluxes are needed to support climate-related policy decisions now and into the future.

The most serious threat to future observational capabilities is that there is currently no planned satellite laser altimeter mission beyond ICESat-2 and GEDI. The continuous acquisition of high-resolution laser altimetry data over the cryosphere and terrestrial ecosystems from space is needed to advance mechanistic understanding of trends and variability in land ice, sea ice and vegetation. The success of satellite laser altimetry for Earth system science has been enhanced by its ability to simultaneously retrieve data over multiple surfaces, which shows the value of using a single measurement approach for multiple applications. Indeed, many of the parameters monitored by laser altimetry are climate variables that are interlinked but are from different disciplines of Earth science. Emerging on-demand rapid data analysis techniques can be used to serve multiple communities simultaneously[214].

We recommend that the various research communities being served by these data should work together across disciplines[215] to identify common measurement requirements and goals. That way, the next generation of satellite laser altimeter missions will be targeting the critical interdisciplinary questions in the Earth system and will be well supported by the community and public.

Published online: 30 January 2024

References

1. *The Status of the Global Climate Observing System 2021: The GCOS Status Report* (WMO, 2021).
2. Dutton, A. et al. Sea-level rise due to polar ice-sheet mass loss during past warm periods. *Science* **349**, aaa4019 (2015).
3. Goosse, H. et al. Quantifying climate feedbacks in polar regions. *Nat. Commun.* **9**, 1919 (2018).
4. Duncanson, L. et al. Aboveground biomass density models for NASA's Global Ecosystem Dynamics Investigation (GEDI) lidar mission. *Remote Sens. Environ.* **270**, 112845 (2022).
5. Ryan, J. C., Smith, L. C., Cooley, S. W., Pitcher, L. H. & Pavelsky, T. M. Global characterization of inland water reservoirs using ICESat-2 altimetry and climate reanalysis. *Geophys. Res. Lett.* https://doi.org/10.1029/2020GL088543 (2020).
6. The Ice, Cloud and land Elevation Satellite-2 (ICESat-2) on-orbit performance, data discoveries and early science. *Geophys. Res. Lett.* https://doi.org/10.1002/(ISSN)1944-8007.ICESAT2 (2022).
7. Schutz, B. E., Zwally, H. J., Shuman, C. A., Hancock, D. & DiMarzio, J. P. Overview of the ICESat mission. *Geophys. Res. Lett.* **32**, L21S01 (2005).
8. Markus, T. et al. The Ice, Cloud, and Land Elevation Satellite-2 (ICESat-2): science requirements, concept, and implementation. *Remote Sens. Environ.* **190**, 260–273 (2017).
9. Dubayah, R. et al. The Global Ecosystem Dynamics Investigation: high-resolution laser ranging of the Earth's forests and topography. *Sci. Remote Sens.* **1**, 100002 (2020).
10. Shan, J. & Toth, C. K. *Topographic Laser Ranging and Scanning: Principles and Processing* (CRC Press, 2018).
11. Zhou, H., Chen, Y., Hyyppä, J. & Li, S. An overview of the laser ranging method of space laser altimeter. *Infrared Phys. Technol.* **86**, 147–158 (2017).
12. Fu, L.-L. & Cazenave, A. *Satellite Altimetry and Earth Sciences: A Handbook of Techniques and Applications* (Elsevier, 2000).
13. Harding, D. J. ICESat waveform measurements of within-footprint topographic relief and vegetation vertical structure. *Geophys. Res. Lett.* **32**, L21S10 (2005).
14. Degnan, J. J. Photon-counting multikilohertz microlaser altimeters for airborne and spaceborne topographic measurements. *J. Geodyn.* **34**, 503–549 (2002).
15. Robin, G. D. Q., Drewry, D. J. & Squire, V. A. Satellite observations of polar ice fields. *Phil. Trans. R. Soc. Lond. A* **309**, 447–461 (1983).
16. Fu, L.-L. et al. TOPEX/POSEIDON mission overview. *J. Geophys. Res.* **99**, 24369 (1994).
17. Brooks, R. L., Campbell, W. J., Ramseier, R. O., Stanley, H. R. & Zwally, H. J. Ice sheet topography by satellite altimetry. *Nature* **274**, 539–543 (1978).
18. Brooks, R. L., Williams, R. S. Jr, Ferrigno, J. G. & Krabill, W. B. in *Antarctic Earth Science* (eds Oliver, R. L. et al.) 441–445 (Cambridge Univ. Press, 1983).
19. Benveniste, J. Strategy for ENVISAT radar altimetry cross-calibration and validation. In *Proc. IGARSS 2000. Taking the Pulse of the Planet: The Role of Remote Sensing in Managing the Environment* 2730–2732 (IEEE, 2000).
20. Wingham, D. J., Ridout, A. J., Scharroo, R., Arthern, R. J. & Shum, C. K. Antarctic elevation change from 1992 to 1996. *Science* **282**, 456–458 (1998).
21. Laxon, S., Peacock, N. & Smith, D. High interannual variability of sea ice thickness in the Arctic region. *Nature* **425**, 947–950 (2003).
22. Brenner, A. C., DiMarzio, J. P. & Zwally, H. J. Precision and accuracy of satellite radar and laser altimeter data over the continental ice sheets. *IEEE Trans. Geosci. Remote Sens.* **45**, 321–331 (2007).
23. Scott, R. F. et al. A comparison of the performance of the ice and ocean tracking modes of the ERS-1 radar altimeter over non-ocean surfaces. *Geophys. Res. Lett.* **21**, 553–556 (1994).
24. Davis, C. H. & Moore, R. K. A combined surface- and volume-scattering model for ice-sheet radar altimetry. *J. Glaciol.* **39**, 675–686 (1993).
25. Magruder, L., Neuenschwander, A. & Klotz, B. Digital terrain model elevation corrections using space-based imagery and ICESat-2 laser altimetry. *Remote Sens. Environ.* **264**, 112621 (2021).
26. Giles, K. A., Laxon, S. W. & Ridout, A. L. Circumpolar thinning of Arctic sea ice following the 2007 record ice extent minimum. *Geophys. Res. Lett.* **35**, L22502 (2008).
27. Drinkwater, M. R., Francis, R., Ratier, G. & Wingham, D. J. The European Space Agency's Earth Explorer Mission CryoSat: measuring variability in the cryosphere. *Ann. Glaciol.* **39**, 313–320 (2004).
28. Zwally, H. J. et al. ICESat's laser measurements of polar ice, atmosphere, ocean, and land. *J. Geodyn.* **34**, 405–445 (2002).
29. Spinhirne, J. D., Palm, S. P. & Hart, W. D. Antarctica cloud cover for October 2003 from GLAS satellite lidar profiling. *Geophys. Res. Lett.* https://doi.org/10.1029/2005GL023782 (2005).
30. Abshire, J. B. et al. Geoscience laser altimeter system (GLAS) on the ICESat mission: on-orbit measurement performance. *Geophys. Res. Lett.* **32**, L21S02 (2005).
31. Schenk, T. & Csatho, B. A new methodology for detecting ice sheet surface elevation changes from laser altimetry data. *IEEE Trans. Geosci. Remote Sensing* **50**, 3302–3316 (2012).
32. Fricker, H. A. Assessment of ICESat performance at the salar de Uyuni, Bolivia. *Geophys. Res. Lett.* **32**, L21S06 (2005).
33. Magruder, L., Silverberg, E., Webb, C. & Schutz, B. In situ timing and pointing verification of the ICESat altimeter using a ground-based system. *Geophys. Res. Lett.* **32**, L21S04 (2005).
34. Gardner, A. S. et al. A reconciled estimate of glacier contributions to sea level rise: 2003 to 2009. *Science* **340**, 852–857 (2013).
35. Pritchard, H. D., Arthern, R. J., Vaughan, D. G. & Edwards, L. A. Extensive dynamic thinning on the margins of the Greenland and Antarctic ice sheets. *Nature* **461**, 971–975 (2009).
36. Pritchard, H. D. et al. Antarctic ice-sheet loss driven by basal melting of ice shelves. *Nature* **484**, 502–505 (2012).
37. Fricker, H. A., Scambos, T., Bindschadler, R. & Padman, L. An active subglacial water system in West Antarctica mapped from space. *Science* **315**, 1544–1548 (2007).
38. Kwok, R. et al. Thinning and volume loss of the Arctic Ocean sea ice cover: 2003–2008. *J. Geophys. Res.* **114**, C07005 (2009).
39. Kurtz, N. T. & Markus, T. Satellite observations of Antarctic sea ice thickness and volume. *J. Geophys. Res.* https://doi.org/10.1029/2012JC008141 (2012).
40. Lefsky, M. A. et al. Estimates of forest canopy height and aboveground biomass using ICESat. *Geophys. Res. Lett.* **32**, GL023971 (2005).
41. Mitchard, E. T. A. The tropical forest carbon cycle and climate change. *Nature* **559**, 527–534 (2018).
42. Saatchi, S. S. et al. Benchmark map of forest carbon stocks in tropical regions across three continents. *Proc. Natl Acad. Sci. USA* **108**, 9899–9904 (2011).
43. Baccini, A. et al. Estimated carbon dioxide emissions from tropical deforestation improved by carbon-density maps. *Nat. Clim. Change* **2**, 182–185 (2012).
44. Wang, L. & Dessler, A. E. Instantaneous cloud overlap statistics in the tropical area revealed by ICESat/GLAS data. *Geophys. Res. Lett.* **33**, L15804 (2006).
45. O'Loughlin, F. E., Neal, J., Yamazaki, D. & Bates, P. D. ICESat-derived inland water surface spot heights. *Water Resour. Res.* **52**, 3276–3284 (2016).
46. National Research Council. *Earth Science and Applications from Space: National Imperatives for the Next Decade and Beyond*. https://nap.nationalacademies.org/read/11820/chapter/1 (National Academies Press, 2007).
47. Martino, A. J., Neumann, T. A., Kurtz, N. T. & McLennan, D. ICESat-2 mission overview and early performance. In *Sensors, Systems, and Next-Generation Satellites XXII* (eds Neeck, S. P. et al.) 11 (SPIE, 2019).
48. Abdalati, W. et al. The ICESat-2 laser altimetry mission. *Proc. IEEE* **98**, 735–751 (2010).
49. Smith, B. et al. Pervasive ice sheet mass loss reflects competing ocean and atmosphere processes. *Science* **368**, 1239–1242 (2020).
50. Dubayah, R. et al. GEDI launches a new era of biomass inference from space. *Environ. Res. Lett.* **17**, 095001 (2022).
51. Brunt, K. M., Neumann, T. A. & Smith, B. E. Assessment of ICESat-2 ice sheet surface heights, based on comparisons over the interior of the Antarctic Ice Sheet. *Geophys. Res. Lett.* **46**, 13072–13078 (2019).
52. Kwok, R. et al. Surface height and sea ice freeboard of the arctic ocean from ICESat-2: characteristics and early results. *J. Geophys. Res. Oceans* **124**, 6942–6959 (2019).
53. Farrell, S. L., Duncan, K., Buckley, E. M., Richter-Menge, J. & Li, R. Mapping sea ice surface topography in high fidelity with ICESat-2. *Geophys. Res. Lett.* https://doi.org/10.1029/2020GL090708 (2020).
54. Neuenschwander, A. L. & Magruder, L. A. Canopy and terrain height retrievals with ICESat-2: a first look. *Remote Sensing* **11**, 1721 (2019).
55. Thomas, N. et al. Space-borne cloud-native satellite-derived bathymetry (SDB) models using ICESat-2 and Sentinel-2. *Geophys. Res. Lett.* https://doi.org/10.1002/essoar.10504452.1 (2021).
56. Fricker, H. A. et al. ICESat-2 meltwater depth estimates: application to surface melt on amery ice shelf, East Antarctica. *Geophys. Res. Lett.* https://doi.org/10.1029/2020GL090550 (2021).
57. Zhu, X. et al. Consistency analysis of forest height retrievals between GEDI and ICESat-2. *Remote Sens. Environ.* **281**, 113244 (2022).
58. IPCC *Special Report on the Ocean and Cryosphere in a Changing Climate* (eds Pörtner, H. O. et al.) (Cambridge Univ. Press, 2022).
59. IPCC *Climate Change 2021: The Physical Science Basis* (eds Masson-Delmotte, V. et al.) (Cambridge Univ. Press, 2023).
60. Parkinson, C. L. Global sea ice coverage from satellite data: annual cycle and 35-yr trends. *J. Clim.* **27**, 9377–9382 (2014).
61. Worby, A. P. et al. Thickness distribution of Antarctic sea ice. *J. Geophys. Res.* **113**, C05S92 (2008).
62. Rothrock, D. A., Yu, Y. & Maykut, G. A. Thinning of the Arctic sea-ice cover. *Geophys. Res. Lett.* **26**, 3469–3472 (1999).
63. Haas, C. et al. Reduced ice thickness in Arctic transpolar drift favors rapid ice retreat. *Geophys. Res. Lett.* **35**, L17501 (2008).
64. Kacimi, S. & Kwok, R. Arctic snow depth, ice thickness, and volume from ICESat-2 and CryoSat-2: 2018–2021. *Geophys. Res. Lett.* https://doi.org/10.1029/2021GL097448 (2022).
65. Ricker, R. et al. Evidence for an increasing role of ocean heat in Arctic winter sea ice growth. *J. Clim.* **34**, 1–42 (2021).
66. Eicken, H., Lovecraft, A. L. & Druckenmiller, M. L. Sea-ice system services: a framework to help identify and meet information needs relevant for observing networks. *Arctic* **62**, 119–136 (2009).

67. Kwok, R., Zwally, H. J. & Yi, D. ICESat observations of Arctic sea ice: a first look. *Geophys. Res. Lett.* **31**, 2004GL020309 (2004).
68. Thoman, R. L. et al. The Arctic. *Bull. Am. Meteorol. Soc.* **103**, S257–S306 (2022).
69. Meier, W. N. et al. Arctic sea ice in transformation: a review of recent observed changes and impacts on biology and human activity. *Rev. Geophys.* **52**, 185–217 (2014).
70. Farrell, S. L., Laxon, S. W., McAdoo, D. C., Yi, D. & Zwally, H. J. Five years of Arctic sea ice freeboard measurements from the Ice, Cloud and land Elevation Satellite. *J. Geophys. Res.* **114**, C04008 (2009).
71. Comiso, J. C., Parkinson, C. L., Gersten, R. & Stock, L. Accelerated decline in the Arctic sea ice cover. *Geophys. Res. Lett.* **35**, L01703 (2008).
72. Kurtz, N. T., Markus, T., Farrell, S. L., Worthen, D. L. & Boisvert, L. N. Observations of recent Arctic sea ice volume loss and its impact on ocean–atmosphere energy exchange and ice production. *J. Geophys. Res.* **116**, C04015 (2011).
73. Laxon, S. W. et al. CryoSat-2 estimates of Arctic sea ice thickness and volume. *Geophys. Res. Lett.* **40**, 732–737 (2013).
74. Fredensborg Hansen, R. M., Rinne, E., Farrell, S. L. & Skourup, H. Estimation of degree of sea ice ridging in the Bay of Bothnia based on geolocated photon heights from ICESat-2. *Cryosphere* **15**, 2511–2529 (2021).
75. Buckley, E. M. et al. Observing the evolution of summer melt on multiyear sea ice with ICESat-2 and Sentinel-2. *The Cryosphere* **17**, 3695–3719 (2023).
76. Duncan, K. & Farrell, S. L. Determining variability in Arctic Sea ice pressure ridge topography with ICESat-2. *Geophys. Res. Lett.* https://doi.org/10.1029/2022GL100272 (2022).
77. Tilling, R., Kurtz, N. T., Bagnardi, M., Petty, A. A. & Kwok, R. Detection of melt ponds on Arctic summer sea ice from ICESat-2. *Geophys. Res. Lett.* https://doi.org/10.1029/2020GL090644 (2020).
78. Eayrs, C., Li, X., Raphael, M. N. & Holland, D. M. Rapid decline in Antarctic sea ice in recent years hints at future change. *Nat. Geosci.* **14**, 460–464 (2021).
79. Zwally, H. J., Yi, D., Kwok, R. & Zhao, Y. ICESat measurements of sea ice freeboard and estimates of sea ice thickness in the Weddell Sea. *J. Geophys. Res.* **113**, C02S15 (2008).
80. Fons, S. W. & Kurtz, N. T. Retrieval of snow freeboard of Antarctic sea ice using waveform fitting of CryoSat-2 returns. *Cryosphere* **13**, 861–878 (2019).
81. Yi, D., Zwally, H. J. & Robbins, J. W. ICESat observations of seasonal and interannual variations of sea-ice freeboard and estimated thickness in the Weddell Sea, Antarctica (2003–2009). *Ann. Glaciol.* **52**, 43–51 (2011).
82. Kacimi, S. & Kwok, R. The Antarctic sea ice cover from ICESat-2 and CryoSat-2: freeboard, snow depth, and ice thickness. *Cryosphere* **14**, 4453–4474 (2020).
83. Horvat, C., Blanchard-Wrigglesworth, E. & Petty, A. Observing waves in sea ice with ICESat-2. *Geophys. Res. Lett.* https://doi.org/10.1029/2020GL087629 (2020).
84. Bisson, K. M. & Cael, B. B. How are under ice phytoplankton related to sea ice in the Southern Ocean? *Geophys. Res. Lett.* https://doi.org/10.1029/2021GL095051 (2021).
85. Otosaka, I. N. et al. Mass balance of the Greenland and Antarctic ice sheets from 1992 to 2020. *Earth Syst. Sci. Data* **15**, 1597–1616 (2023).
86. Hugonnet, R. et al. Accelerated global glacier mass loss in the early twenty-first century. *Nature* **592**, 726–731 (2021).
87. Shepherd, A. et al. A reconciled estimate of ice-sheet mass balance. *Science* **338**, 1183–1189 (2012).
88. The IMBIE team. Mass balance of the Antarctic Ice Sheet from 1992 to 2017. *Nature* **558**, 219–222 (2018).
89. Shepherd, A., Fricker, H. A. & Farrell, S. L. Trends and connections across the Antarctic cryosphere. *Nature* **558**, 223–232 (2018).
90. Csatho, B. M. et al. Laser altimetry reveals complex pattern of Greenland Ice Sheet dynamics. *Proc. Natl Acad. Sci. USA* **111**, 18478–18483 (2014).
91. Porter, D. F. et al. Bathymetric control of tidewater glacier mass loss in northwest Greenland. *Earth Planet. Sci. Lett.* **401**, 40–46 (2014).
92. Korsgaard, N. J. et al. Digital elevation model and orthophotographs of Greenland based on aerial photographs from 1978–1987. *Sci. Data* **3**, 160032 (2016).
93. Spada, G. et al. Greenland uplift and regional sea level changes from ICESat observations and GIA modelling: Greenland uplift and sea level change. *Geophys. J. Int.* **189**, 1457–1474 (2012).
94. Larour, E. et al. Inferred basal friction and surface mass balance of the Northeast Greenland Ice Stream using data assimilation of ICESat (Ice Cloud and land Elevation Satellite) surface altimetry and ISSM (Ice Sheet System Model). *Cryosphere* **8**, 2335–2351 (2014).
95. Moholdt, G., Padman, L. & Fricker, H. A. Basal mass budget of Ross and Filchner-Ronne ice shelves, Antarctica, derived from Lagrangian analysis of ICESat altimetry. *J. Geophys. Res.: Earth Surface* **119**, 2361–2380 (2014).
96. Horgan, H. J., Walker, R. T., Anandakrishnan, S. & Alley, R. B. Surface elevation changes at the front of the Ross Ice Shelf: implications for basal melting. *J. Geophys. Res.* **116**, C02005 (2011).
97. Fricker, H. A. & Padman, L. Ice shelf grounding zone structure from ICESat laser altimetry. *Geophys. Res. Lett.* **33**, L15502 (2006).
98. Brunt, K. M., Fricker, H. A. & Padman, L. Analysis of ice plains of the Filchner–Ronne Ice Shelf, Antarctica, using ICESat laser altimetry. *J. Glaciol.* **57**, 965–975 (2011).
99. Marsh, O. J. et al. High basal melting forming a channel at the grounding line of Ross Ice Shelf, Antarctica. *Geophys. Res. Lett.* **43**, 250–255 (2016).
100. Smith, B. E., Fricker, H. A., Joughin, I. R. & Tulaczyk, S. An inventory of active subglacial lakes in Antarctica detected by ICESat (2003–2008). *J. Glaciol.* **55**, 573–595 (2009).
101. Gudmundsson, G. H., Paolo, F. S., Adusumilli, S. & Fricker, H. A. Instantaneous Antarctic ice sheet mass loss driven by thinning ice shelves. *Geophys. Res. Lett.* **46**, 13903–13909 (2019).
102. Taubenberger, C. J., Felikson, D. & Neumann, T. Brief communication: preliminary ICESat-2 (Ice, Cloud and land Elevation Satellite-2) measurements of outlet glaciers reveal heterogeneous patterns of seasonal dynamic thickness change. *Cryosphere* **16**, 1341–1348 (2022).
103. Clem, K. R. et al. Antarctica and the Southern Ocean. *Bull. Am. Meteorol. Soc.* **103**, S307–S340 (2022).
104. Smith, B. E. et al. Evaluating Greenland surface-mass-balance and firn-densification data using ICESat-2 altimetry. *Cryosphere* **17**, 789–808 (2023).
105. Adusumilli, S., Fish, M., Fricker, H. A. & Medley, B. Atmospheric river precipitation contributed to rapid increases in surface height of the West Antarctic Ice Sheet in 2019. *Geophys. Res. Lett.* https://doi.org/10.1029/2020GL091076 (2021).
106. Herzfeld, U. C., Trantow, T., Lawson, M., Hans, J. & Medley, G. Surface heights and crevasse morphologies of surging and fast-moving glaciers from ICESat-2 laser altimeter data — application of the density-dimension algorithm (DDA-ice) and evaluation using airborne altimeter and Planet SkySat data. *Sci. Remote Sens.* **3**, 100013 (2021).
107. Becker, M. K. et al. Buoyancy-driven flexure at the front of Ross Ice Shelf, Antarctica, observed with ICESat-2 laser altimetry. *Geophys. Res. Lett.* https://doi.org/10.1029/2020GL091207 (2021).
108. Walker, C. C., Becker, M. K. & Fricker, H. A. A high resolution, three-dimensional view of the D-28 calving event from Amery Ice Shelf with ICESat-2 and satellite imagery. *Geophys. Res. Lett.* https://doi.org/10.1029/2020GL091200 (2021).
109. Li, T., Dawson, G., Chuter, S. & Bamber, J. A high-resolution Antarctic grounding zone product from ICESat-2 laser altimetry. *Earth Syst. Sci. Data* **14**, 535–557 (2022).
110. Freer, B. I. D., Marsh, O. J., Hogg, A. E., Fricker, H. A. & Padman, L. Modes of Antarctic tidal grounding line migration revealed by ICESat-2 laser altimetry. *The Cryosphere* **17**, 4079–4101 (2023).
111. Chartrand, A. M. & Howat, I. M. Basal channel evolution on the Getz Ice Shelf, West Antarctica. *J. Geophys. Res.: Earth Surface* https://doi.org/10.1029/2019JF005293 (2020).
112. Narkevic, A., Csatho, B. & Schenk, T. Rapid basal channel growth beneath Greenland's longest floating ice shelf. *Geophys. Res. Lett.* **50**, e2023GL103226 (2023).
113. Warner, R. C. et al. Rapid formation of an ice doline on Amery Ice Shelf, East Antarctica. *Geophys. Res. Lett.* **48**, e2020GL091095 (2021).
114. Wild, C. T. et al. Weakening of the pinning point buttressing Thwaites Glacier, West Antarctica. *Cryosphere* **16**, 397–417 (2022).
115. Siegfried, M. R. & Fricker, H. A. Illuminating active subglacial lake processes with ICESat-2 laser altimetry. *Geophys. Res. Lett.* https://doi.org/10.1029/2020GL091089 (2021).
116. Datta, R. T. & Wouters, B. Supraglacial lake bathymetry automatically derived from ICESat-2 constraining lake depth estimates from multi-source satellite imagery. *Cryosphere* **15**, 5115–5132 (2021).
117. Jin, S., Zhang, T. Y. & Zou, F. Glacial density and GIA in Alaska estimated from ICESat, GPS and GRACE measurements: glacial density and GIA in Alaska. *J. Geophys. Res. Earth Surf.* **122**, 76–90 (2017).
118. Kääb, A., Berthier, E., Nuth, C., Gardelle, J. & Arnaud, Y. Contrasting patterns of early twenty-first-century glacier mass change in the Himalayas. *Nature* **488**, 495–498 (2012).
119. Bolch, T. et al. Mass loss of Greenland's glaciers and ice caps 2003–2008 revealed from ICESat laser altimetry data. *Geophys. Res. Lett.* **40**, 875–881 (2013).
120. Moholdt, G., Wouters, B. & Gardner, A. S. Recent mass changes of glaciers in the Russian High Arctic. *Geophys. Res. Lett.* https://doi.org/10.1029/2012GL051466 (2012).
121. Nuth, C., Moholdt, G., Kohler, J., Hagen, J. O. & Kääb, A. Svalbard glacier elevation changes and contribution to sea level rise. *J. Geophys. Res.* **115**, 2008JF001223 (2010).
122. Khan, S. A. et al. Accelerating ice loss from peripheral glaciers in North Greenland. *Geophys. Res. Lett.* https://doi.org/10.1029/2022GL098915 (2022).
123. Wang, J., Yang, Y., Wang, C. & Li, L. Accelerated glacier mass loss over Svalbard derived from ICESat-2 in 2019–2021. *Atmosphere* **13**, 1255 (2022).
124. Sochor, L., Seehaus, T. & Braun, M. H. Increased ice thinning over Svalbard measured by ICESat/ICESat-2 laser altimetry. *Remote Sens.* **13**, 2089 (2021).
125. Wang, Q., Yi, S. & Sun, W. Continuous estimates of glacier mass balance in high mountain Asia based on ICESat-1,2 and GRACE/GRACE follow-on data. *Geophys. Res. Lett.* https://doi.org/10.1029/2020GL090954 (2021).
126. Wang, Q. & Sun, W. Seasonal cycles of high mountain Asia glacier surface elevation detected by ICESat-2. *J. Geophys. Res. Atmos.* https://doi.org/10.1029/2022JD037501 (2022).
127. Chen, W. et al. Towards ice-thickness inversion: an evaluation of global digital elevation models (DEMs) in the glacierized Tibetan Plateau. *Cryosphere* **16**, 197–218 (2022).
128. Ye, Q. et al. Monitoring glacier thinning rate in Rongbuk catchment on the northern slope of Mt. Qomolangma from 1974 to 2021. *Ecol. Indic.* **144**, 109418 (2022).
129. Friedlingstein, P. et al. Global carbon budget 2022. *Earth System Science Data* **14**, 4811–4900 (2022).
130. Herold, M. et al. The role and need for space-based forest biomass-related measurements in environmental management and policy. *Surv. Geophys.* **40**, 757–778 (2019).
131. Yamazaki, D. et al. A high-accuracy map of global terrain elevations: accurate global terrain elevation map. *Geophys. Res. Lett.* **44**, 5844–5853 (2017).
132. Simard, M., Pinto, N., Fisher, J. B. & Baccini, A. Mapping forest canopy height globally with spaceborne lidar. *J. Geophys. Res.* **116**, G04021 (2011).
133. Duncanson, L. I., Niemann, K. O. & Wulder, M. A. Estimating forest canopy height and terrain relief from GLAS waveform metrics. *Remote Sens. Environ.* **114**, 138–154 (2010).
134. Hilbert, C. & Schmullius, C. Influence of surface topography on ICESat/GLAS forest height estimation and waveform shape. *Remote Sens.* **4**, 2210–2235 (2012).
135. Lang, N. et al. Global canopy height regression and uncertainty estimation from GEDI LIDAR waveforms with deep ensembles. *Remote Sens. Environ.* **268**, 112760 (2022).

136. Healey, S. P., Yang, Z., Gorelick, N. & Ilyushchenko, S. Highly local model calibration with a new GEDI LiDAR asset on Google Earth Engine reduces Landsat forest height signal saturation. *Remote Sens.* **12**, 2840 (2020).
137. Schlund, M., Wenzel, A., Camarretta, N., Stiegler, C. & Erasmi, S. Vegetation canopy height estimation in dynamic tropical landscapes with TanDEM-X supported by GEDI data. *Methods Ecol. Evol*. https://doi.org/10.1111/2041-210X.13933 (2022).
138. Choi, C. et al. Large-scale forest height mapping by combining TanDEM-X and GEDI data. *IEEE J. Sel. Top. Appl. Earth Obs. Remote Sens.* **16**, 2374–2385 (2023).
139. Liu, X. et al. Neural network guided interpolation for mapping canopy height of China's forests by integrating GEDI and ICESat-2 data. *Remote Sens. Environ.* **269**, 112844 (2022).
140. Li, Y. et al. Retrieving low and sparse vegetation heights in desert ecosystems using ICESat-2 ATL03 photon-counting LiDAR data. *IEEE Geosci. Remote Sens. Lett.* https://doi.org/10.1109/LGRS.2022.3194877 (2022).
141. Milenković, M. et al. Dataset for assessing Amazon rainforest regrowth with GEDI and ICESat-2 data. https://doi.org/10.5281/ZENODO.6480488 (2022).
142. Neuenschwander, A., Guenther, E., White, J. C., Duncanson, L. & Montesano, P. Validation of ICESat-2 terrain and canopy heights in boreal forests. *Remote Sens. Environ.* **251**, 112110 (2020).
143. Feng, T. et al. A systematic evaluation of multi-resolution ICESat-2 ATL08 terrain and canopy heights in boreal forests. *Remote Sens. Environ.* **291**, 113570 (2023).
144. Ni, W., Zhang, Z. & Sun, G. Assessment of slope-adaptive metrics of GEDI waveforms for estimations of forest aboveground biomass over mountainous areas. *J. Remote Sens.* **2021**, 2021/9805364 (2021).
145. Rosenqvist, J., Rosenqvist, A. & McDonald, K. C. An analysis of ICESat-2, PALSAR-2 and Sentinel-1 data for the assessment of inundation characteristics in the Amazon Basin. In *IGARSS 2020 — 2020 IEEE International Geoscience and Remote Sensing Symposium*, 5081–5084 (IEEE, 2020).
146. Thomas, N. et al. Seasonal flooding provides limitations and opportunities for ecosystem carbon accounting from space. *Environ. Res. Lett.* **18**, 081002 (2023).
147. Cobb, A. R. et al. Improved terrain estimation from spaceborne lidar in tropical peatlands using spatial filtering. *Sci. Remote Sens.* **7**, 100074 (2023).
148. Urbazaev, M. et al. Assessment of terrain elevation estimates from ICESat-2 and GEDI spaceborne LiDAR missions across different land cover and forest types. *Sci. Remote Sens.* **6**, 100067 (2022).
149. Tang, H., Dubayah, R., Brolly, M., Ganguly, S. & Zhang, G. Large-scale retrieval of leaf area index and vertical foliage profile from the spaceborne waveform lidar (GLAS/ICESat). *Remote Sens. Environ.* **154**, 8–18 (2014).
150. Chen, J. M., Rich, P. M., Gower, S. T., Norman, J. M. & Plummer, S. Leaf area index of boreal forests: theory, techniques, and measurements. *J. Geophys. Res. Atmos.* **102**, 29429–29443 (1997).
151. Drake, J. B. et al. Above-ground biomass estimation in closed canopy Neotropical forests using lidar remote sensing: factors affecting the generality of relationships. *Glob. Ecol. Biogeogr.* **12**, 147–159 (2003).
152. Fatoyinbo, T. E. & Simard, M. Height and biomass of mangroves in Africa from ICESat/GLAS and SRTM. *Int. J. Remote Sens.* **34**, 668–681 (2013).
153. Dolan, K., Masek, J. G., Huang, C. & Sun, G. Regional forest growth rates measured by combining ICESat GLAS and Landsat data. *J. Geophys. Res. Biogeosci.* https://doi.org/10.1029/2008JG000893 (2009).
154. García, M. et al. Characterization of canopy fuels using ICESat/GLAS data. *Remote Sens. Environ.* **123**, 81–89 (2012).
155. Shendryk, Y. Fusing GEDI with Earth observation data for large area aboveground biomass mapping. *Int. J. Appl. Earth Obs. Geoinf.* **115**, 103108 (2022).
156. Bullock, E. L. et al. Estimating aboveground biomass density using hybrid statistical inference with GEDI lidar data and Paraguay's national forest inventory. *Environ. Res. Lett.* **18**, 085001 (2023).
157. Duncanson, L. et al. The effectiveness of global protected areas for climate change mitigation. *Nat. Commun.* **14**, 2908 (2023).
158. Hoffrén, R. et al. Assessing GEDI-NASA system for forest fuels classification using machine learning techniques. *Int. J. Appl. Earth Obs. Geoinf.* **116**, 103175 (2023).
159. Liu, M. & Popescu, S. Estimation of biomass burning emissions by integrating ICESat-2, Landsat 8, and Sentinel-1 data. *Remote Sens. Environ.* **280**, 113172 (2022).
160. Francini, S., D'Amico, G., Vangi, E., Borghi, C. & Chirici, G. Integrating GEDI and landsat: spaceborne lidar and four decades of optical imagery for the analysis of forest disturbances and biomass changes in Italy. *Sensors* **22**, 2015 (2022).
161. Liang, M., Duncanson, L., Silva, J. A. & Sedano, F. Quantifying aboveground biomass dynamics from charcoal degradation in Mozambique using GEDI Lidar and Landsat. *Remote Sens. Environ.* **284**, 113367 (2023).
162. Hakkenberg, C. R., Tang, H., Burns, P. & Goetz, S. J. Canopy structure from space using GEDI lidar. *Front. Ecol. Environ.* **21**, 55–56 (2023).
163. Crockett, E. T. H. et al. Structural and species diversity explain aboveground carbon storage in forests across the United States: evidence from GEDI and forest inventory data. *Remote Sens. Environ.* **295**, 113703 (2023).
164. Torresani, M. et al. LiDAR GEDI derived tree canopy height heterogeneity reveals patterns of biodiversity in forest ecosystems. *Ecol. Inform.* **76**, 102082 (2023).
165. Marselis, S. M., Keil, P., Chase, J. M. & Dubayah, R. The use of GEDI canopy structure for explaining variation in tree species richness in natural forests. *Environ. Res. Lett.* **17**, 045003 (2022).
166. Doughty, C. E. et al. Tropical forests are mainly unstratified especially in Amazonia and regions with lower fertility or higher temperatures. *Environ. Res. Ecol.* **2**, 035002 (2023).
167. Smith, A. B. et al. Spaceborne LiDAR and animal–environment relationships: an assessment for forest carnivores and their prey in the Greater Yellowstone ecosystem. *For. Ecol. Manag.* **520**, 120343 (2022).
168. Burns, P. et al. Incorporating canopy structure from simulated GEDI lidar into bird species distribution models. *Environ. Res. Lett.* **15**, 095002 (2020).
169. Ma, L. et al. Global evaluation of the Ecosystem Demography model (ED v3.0). *Geosci. Model Dev.* **15**, 1971–1994 (2022).
170. Duncanson, L. et al. Forest aboveground biomass estimation with GEDI and ICESat-2 in boreal forests. In *2021 IEEE International Geoscience and Remote Sensing Symposium IGARSS*, 670–672 (IEEE, 2021).
171. Xu, N. et al. Deriving highly accurate shallow water bathymetry from Sentinel-2 and ICESat-2 datasets by a multitemporal stacking method. *IEEE J. Sel. Top. Appl. Earth Obs. Remote Sens.* **14**, 6677–6685 (2021).
172. Buzzanga, B., Heijkoop, E., Hamlington, B. D., Nerem, R. S. & Gardner, A. An assessment of regional ICESat-2 sea-level trends. *Geophys. Res. Lett.* https://doi.org/10.1029/2020GL092327 (2021).
173. Cooley, S. W., Ryan, J. C. & Smith, L. C. Human alteration of global surface water storage variability. *Nature* **591**, 78–81 (2021).
174. Scherer, D., Schwatke, C., Dettmering, D. & Seitz, F. ICESat-2 based river surface slope and its impact on water level time series from satellite altimetry. *Water Resour. Res.* **58**, e2022WR032842 (2022).
175. Parrish, C. E. et al. Validation of ICESat-2 ATLAS bathymetry and analysis of ATLAS's bathymetric mapping performance. *Remote Sens.* **11**, 1634 (2019).
176. Teutschbein, C. & Seibert, J. Bias correction of regional climate model simulations for hydrological climate-change impact studies: review and evaluation of different methods. *J.Hydrol.* **456–457**, 12–29 (2012).
177. Alsdorf, D. E., Rodríguez, E. & Lettenmaier, D. P. Measuring surface water from space. *Rev. Geophys.* **45**, RG2002 (2007).
178. Luo, S. et al. Satellite laser altimetry reveals a net water mass gain in global lakes with spatial heterogeneity in the early 21st century. *Geophys. Res. Lett.* **49**, e2021GL096676 (2022).
179. Birkett, C. M. & Beckley, B. Investigating the performance of the Jason-2/OSTM radar altimeter over lakes and reservoirs. *Mar. Geod.* **33**, 204–238 (2010).
180. Song, C., Huang, B., Ke, L. & Richards, K. S. Seasonal and abrupt changes in the water level of closed lakes on the Tibetan Plateau and implications for climate impacts. *J. Hydrol.* **514**, 131–144 (2014).
181. Song, L. et al. Integrating ICESat-2 altimetry and machine learning to estimate the seasonal water level and storage variations of national-scale lakes in China. *Remote Sens. Environ.* **294**, 113657 (2023).
182. Liu, A., Cheng, X. & Chen, Z. Performance evaluation of GEDI and ICESat-2 laser altimeter data for terrain and canopy height retrievals. *Remote Sens. Environ.* **264**, 112571 (2021).
183. Zhang, Z., Bo, Y., Jin, S., Chen, G. & Dong, Z. Dynamic water level changes in Qinghai Lake from integrating refined ICESat-2 and GEDI altimetry data (2018–2021). *J. Hydrol.* **617**, 129007 (2023).
184. Urban, T. J. & Schutz, B. E. ICESat sea level comparisons. *Geophys. Res. Lett.* **32**, L23S10 (2005).
185. Farrell, S. L. et al. Mean dynamic topography of the Arctic Ocean. *Geophys. Res. Lett.* **39**, 1601 (2012).
186. Forsberg, R. & Skourup, H. Arctic Ocean gravity, geoid and sea-ice freeboard heights from ICESat and GRACE. *Geophys. Res. Lett.* **32**, L21502 (2005).
187. McAdoo, D. C. et al. Gravity of the Arctic Ocean from satellite data with validations using airborne gravimetry: oceanographic implications. *J. Geophys. Res. Oceans* **118**, 917–930 (2013).
188. Padman, L. & Fricker, H. A. Tides on the Ross Ice Shelf observed with ICESat. *Geophys. Res. Lett.* https://doi.org/10.1029/2005GL023214 (2005).
189. Padman, L., Erofeeva, S. Y. & Fricker, H. A. Improving Antarctic tide models by assimilation of ICESat laser altimetry over ice shelves. *Geophys. Res. Lett.* **35**, L22504 (2008).
190. Crooks, S. The effect of sea-level rise on coastal geomorphology: sea-level rise and coastal geomorphology. *Ibis* **146**, 18–20 (2004).
191. Herrmann, J., Magruder, L. A., Markel, J. & Parrish, C. E. Assessing the ability to quantify bathymetric change over time using solely satellite-based measurements. *Remote Sens.* **14**, 1232 (2022).
192. Le Quilleuc, A., Collin, A., Jasinski, M. F. & Devillers, R. Very high-resolution satellite-derived bathymetry and habitat mapping using Pleiades-1 and ICESat-2. *Remote Sens.* **14**, 133 (2021).
193. Syrakov, D., Djolov, G. & Yordanov, D. Incorporation of planetary boundary layer dynamics in a numerical model of long-range air-pollutant transport. *Bound. -Layer Meteorol.* **26**, 1–13 (1983).
194. Kulmala, M. et al. Aerosols, clusters, greenhouse gases, trace gases and boundary-layer dynamics: on feedbacks and interactions. *Bound.-Lay. Meteorol.* **186**, 475–503 (2023).
195. Stephens, G. L. et al. An update on Earth's energy balance in light of the latest global observations. *Nat. Geosci.* **5**, 691–696 (2012).
196. Eguchi, N., Yokota, T. & Inoue, G. Characteristics of cirrus clouds from ICESat/GLAS observations. *Geophys. Res. Lett*. https://doi.org/10.1029/2007GL029529 (2007).
197. Palm, S. P. et al. ICESat-2 atmospheric channel description, data processing and first results. *Earth Space Sci*. https://doi.org/10.1029/2020EA001470 (2021).
198. Palm, S. P., Selmer, P., Yorks, J., Nicholls, S. & Nowottnick, E. Planetary boundary layer height estimates from ICESat-2 and CATS backscatter measurements. *Front. Remote Sens.* **2**, 716951 (2021).

199. Herzfeld, U. et al. Detection and height measurement of tenuous clouds and blowing snow in ICESat-2 ATLAS data. *Geophys. Res. Lett.* https://doi.org/10.1029/2021GL093473 (2021).
200. Duda, D. P., Spinhirne, J. D. & Eloranta, E. W. Atmospheric multiple scattering effects on GLAS altimetry. I. Calculations of single pulse bias. *IEEE Trans. Geosci. Remote Sens.* **39**, 92–101 (2001).
201. Yang, Y., Marshak, A., Palm, S. P., Varnai, T. & Wiscombe, W. J. Cloud impact on surface altimetry from a spaceborne 532-nm micropulse photon-counting lidar: system modeling for cloudy and clear atmospheres. *IEEE Trans. Geosci. Remote Sens.* **49**, 4910–4919 (2011).
202. Hansen, J. et al. Earth's energy imbalance: confirmation and implications. *Science* **308**, 1431–1435 (2005).
203. *Atmospheric Aerosols: Life Cycles and Effects on Air Quality and Climate* (Wiley, 2017).
204. Hoff, R. M., Palm, S. P., Engel-Cox, J. A. & Spinhirne, J. GLAS long-range transport observation of the 2003 California forest fire plumes to the northeastern US. *Geophys. Res. Lett.* **32**, n/a–n/a (2005).
205. Wyngaard, J. C. Structure of the planetary boundary layer and implications for its modeling. *J. Appl. Meteorol. Climatol.* **24**, 1131–1142 (1985).
206. McGrath-Spangler, E. L. & Denning, A. S. Global seasonal variations of midday planetary boundary layer depth from CALIPSO space-borne LIDAR: variations of PBL depth from CALIPSO. *J. Geophys. Res. Atmos.* **118**, 1226–1233 (2013).
207. Teixeira, J. et al. *Toward a Global Planetary Boundary Layer Observing System: The NASA PBL Incubation Study Team Report* (NASA, 2021).
208. Hancock, S., McGrath, C., Lowe, C., Davenport, I. & Woodhouse, I. Requirements for a global lidar system: spaceborne lidar with wall-to-wall coverage. *R. Soc. Open Sci.* **8**, 211166 (2021).
209. Berthier, E. et al. Measuring glacier mass changes from space — a review. *Rep. Prog. Phys.* https://doi.org/10.1088/1361-6633/acaf8e (2023).
210. Ricker, R. et al. Linking scales of sea ice surface topography: evaluation of ICESat-2 measurements with coincident helicopter laser scanning during MOSAiC. *The Cryosphere* **17**, 1411–1429 (2022).
211. Roy, D. P., Kashongwe, H. B. & Armston, J. The impact of geolocation uncertainty on GEDI tropical forest canopy height estimation and change monitoring. *Sci. Remote Sens.* **4**, 100024 (2021).
212. Tang, H. et al. Evaluating and mitigating the impact of systematic geolocation error on canopy height measurement performance of GEDI. *Remote Sens. Environ.* **291**, 113571 (2023).
213. Kern, M. et al. The copernicus polar ice and snow topography altimeter (CRISTAL) high-priority candidate mission. *Cryosphere* **14**, 2235–2251 (2020).
214. Shean, D. et al. SlideRule: enabling rapid, scalable, open science for the NASA ICESat-2 mission and beyond. *J. Open Source Softw.* **8**, 4982 (2023).
215. Donnellan, A. et al. *Observing Earth's Changing Surface Topography and Vegetation Structure: A Framework for the Decade* NASA Surface Topography and Vegetation Incubation Study (NASA, 2021)
216. Herzfeld, U. C., Lawson, M., Trantow, T. & Nylen, T. Airborne validation of ICESat-2 ATLAS data over crevassed surfaces and other complex glacial environments: results from experiments of laser altimeter and kinematic GPS data collection from a helicopter over a surging arctic glacier (Negribreen, Svalbard). *Remote Sens.* **14**, 1185 (2022).
217. Thomas, N. et al. A purely spaceborne open source approach for regional bathymetry mapping. *IEEE Trans. Geosci. Remote Sens.* https://doi.org/10.1109/TGRS.2022.3192825 (2022).
218. Palm, S. P., Benedetti, A. & Spinhirne, J. Validation of ECMWF global forecast model parameters using GLAS atmospheric channel measurements. *Geophys. Res. Lett.*https://doi.org/10.1029/2005GL023535 (2005).
219. Luthcke, S. B. Reduction of ICESat systematic geolocation errors and the impact on ice sheet elevation change detection. *Geophys. Res. Lett.* **32**, L21S05 (2005).
220. Luthcke, S. B. et al. ICESat-2 pointing calibration and geolocation performance. *Earth Space Sci.* https://doi.org/10.1029/2020EA001494 (2021).

Acknowledgements
We thank the ICESat, ICESat-2 and GEDI project science offices, and all of the scientists and engineers who have worked on understanding laser altimetry data to push the technology and science results forward. We express special thanks to the following for their contributions to the figures: C. Smith (Fig. 1), V. Leitold (Fig. 3) and N. Thomas (Fig. 4b) (all Univ. Maryland); I. Parmuzin (Univ. Buffalo; Fig. 2); U. Herzfeld (Univ. Colorado Boulder; Fig. 2c); and H. J. Zwally (Fig. 2b) and S. Palm (Fig. 5) (both NASA Goddard Space Flight Center). All authors received funding from NASA through the ICESat-2 mission as members of the Science Team. L.D. and A.N. are also funded through NASA's ABoVE science team. which focuses on mapping boreal biomass estimates. L.D. is also funded by the GEDI Science Team.

Author contributions
The original concept for the manuscript included L.A.M., S.L.F., H.A.F. and A.N., which resulted in the submission of the synopsis for initial review. All authors contributed to the analysis, writing and editing of the full manuscript.

Competing interests
The authors declare no competing interests.

Additional information
Peer review information *Nature Reviews Earth & Environment* thanks Yuekui Yang, Hao Tang and the other, anonymous, reviewer(s) for their contribution to the peer review of this work.

Publisher's note Springer Nature remains neutral with regard to jurisdictional claims in published maps and institutional affiliations.